Molecular Cell

Article

Cryoelectron tomography reveals the multiplex anatomy of condensed native chromatin and its unfolding by histone citrullination

Graphical abstract

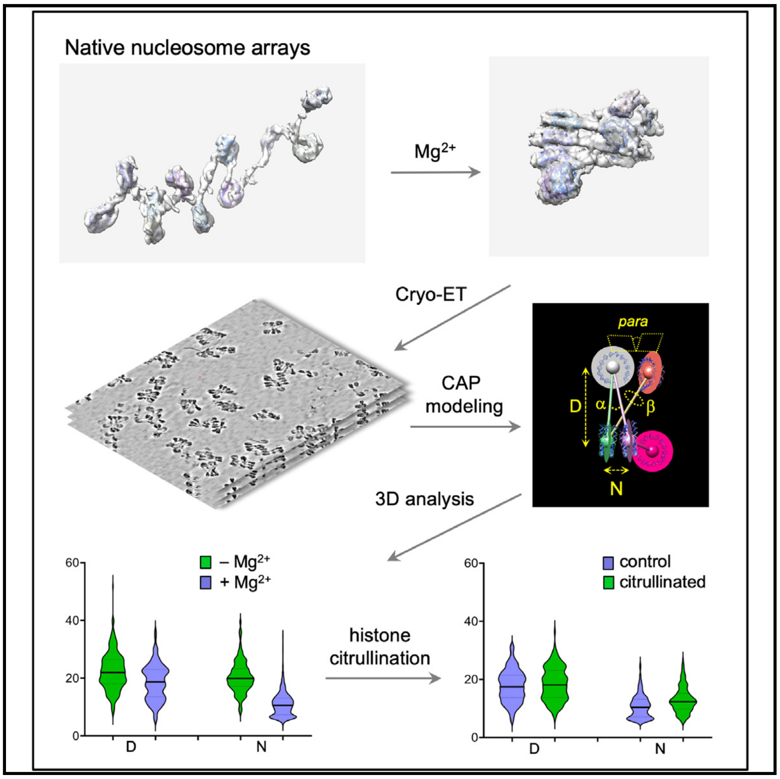

Highlights

- Native human chromatin is analyzed by cryo-ET in open and condensed states
- Condensed native chromatin acquires nucleosome stacks with irregular trajectories
- Histone citrullination inhibits stacking and partially unfolds native chromatin
- Reconstituted chromatin packs uniformly and fully unfolds upon citrullination

Authors

Nathan Jentink, Carson Purnell, Brianna Kable, Matthew T. Swulius, Sergei A. Grigoryev

Correspondence

mts286@psu.edu (M.T.S.),
sag17@psu.edu (S.A.G.)

In brief

Combining cryo-ET methodology with deep denoising and stereology, Jentink et al. analyze individual nucleosomes in condensed human chromatin and quantitively assess its structural transitions. This study provides mechanistic insights into chromatin unfolding by histone citrullination and reveals major structural differences between native chromatin and reconstituted regular nucleosome arrays.

Jentink et al., 2023, Molecular Cell *83*, 3236–3252
September 21, 2023 © 2023 The Authors. Published by Elsevier Inc.
https://doi.org/10.1016/j.molcel.2023.08.017

CellPress
OPEN ACCESS

Molecular Cell

Article

Cryoelectron tomography reveals the multiplex anatomy of condensed native chromatin and its unfolding by histone citrullination

Nathan Jentink,[1] Carson Purnell,[1] Brianna Kable,[1] Matthew T. Swulius,[1,*] and Sergei A. Grigoryev[1,2,*]
[1]Penn State University College of Medicine, Department of Biochemistry & Molecular Biology, H171, Milton S. Hershey Medical Center, P.O. Box 850, 500 University Drive, Hershey, PA 17033, USA
[2]Lead contact
*Correspondence: mts286@psu.edu (M.T.S.), sag17@psu.edu (S.A.G.)
https://doi.org/10.1016/j.molcel.2023.08.017

SUMMARY

Nucleosome chains fold and self-associate to form higher-order structures whose internal organization is unknown. Here, cryoelectron tomography (cryo-ET) of native human chromatin reveals intrinsic folding motifs such as (1) non-uniform nucleosome stacking, (2) intermittent parallel and perpendicular orientations of adjacent nucleosome planes, and (3) a regressive nucleosome chain path, which deviates from the direct zigzag topology seen in reconstituted nucleosomal arrays. By examining the self-associated structures, we observed prominent nucleosome stacking in *cis* and anti-parallel nucleosome interactions, which are consistent with partial nucleosome interdigitation in *trans*. Histone citrullination strongly inhibits nucleosome stacking and self-association with a modest effect on chromatin folding, whereas the reconstituted arrays undergo a dramatic unfolding into open zigzag chains induced by histone citrullination. This study sheds light on the internal structure of compact chromatin nanoparticles and suggests a mechanism for how epigenetic changes in chromatin folding are retained across both open and condensed forms.

INTRODUCTION

The DNA in eukaryotic chromatin is repeatedly coiled around histone proteins, forming arrays of 10 nm nucleosomes. Each nucleosome contains a core of about 147 bp of DNA that makes approximately 1.7 left superhelical turns around an octamer of histones H2A, H2B, H3, and H4.[1,2] Nucleosome “beads” are connected by extended linker DNA “strings” (10–100 bp in length) into “beads-on-a-string” nucleosome arrays. These arrays are packed through chromatin higher-order folding mechanisms to achieve a 400- to 1,000-fold compaction of DNA in interphase chromatin[3] and a 10,000-fold compaction in condensed metaphase chromosomes.[4] Chromatin higher-order folding limits DNA accessibility for transcription factors[5,6] and DNA repair machinery[7] and mediates chromosomal integrity during cell division.[8] Solving the 3D organization of native nucleosome arrays in their condensed states and understanding molecular mechanism(s) driving tight nucleosome packing would bring about a fundamental advance in understanding the processes underlying epigenetic gene regulation and chromosomal stability.

Chromatin higher-order folding has been suggested to comprise a hierarchy of structural levels. Nucleosome arrays (primary level) first fold longitudinally into 30-nm chromatin fibers (secondary level) and then self-associate latitudinally to form tertiary structures.[9] The 30-nm chromatin fibers have been observed in the nuclei of some terminally differentiated cells[10–12] and nucleosome arrays reconstituted with regular nucleosome positioning sequences showing a prominent secondary level folding along the two-start zigzag.[13–18] However, depending on the nucleosome linker length,[14] reconstituted chromatin may be strikingly different from the two-start zigzag, as was recently observed for nucleosomes reconstituted on telomeric DNA.[19] Moreover, despite many years of intensive studies, the existence of any regularly folded structures above the primary nucleosome level remains elusive in most eukaryotic cells,[20–28] and the tertiary-level nucleosome condensates did not show any distinct secondary structures as their intermediates.[29] These nucleosome condensates appeared to be remarkably fluid and displayed properties of either liquid droplets or semi-solid hydrogels, depending on the experimental conditions and the state of histone modification.[30–32]

Nevertheless, capturing nucleosome interactions in mammalian cell nuclei[33–36] showed a distinct pattern of proximities consistent with two-start zigzag folding. Furthermore, short nucleosome clusters, or nanodomains, were observed by super-resolution microscopy,[27,37,38] and some higher-order folds, loops, and hubs formed by closely juxtaposed nucleosomes were observed by electron tomography,[25] indicating that despite the absence of the long regular fibers, some discrete elements of

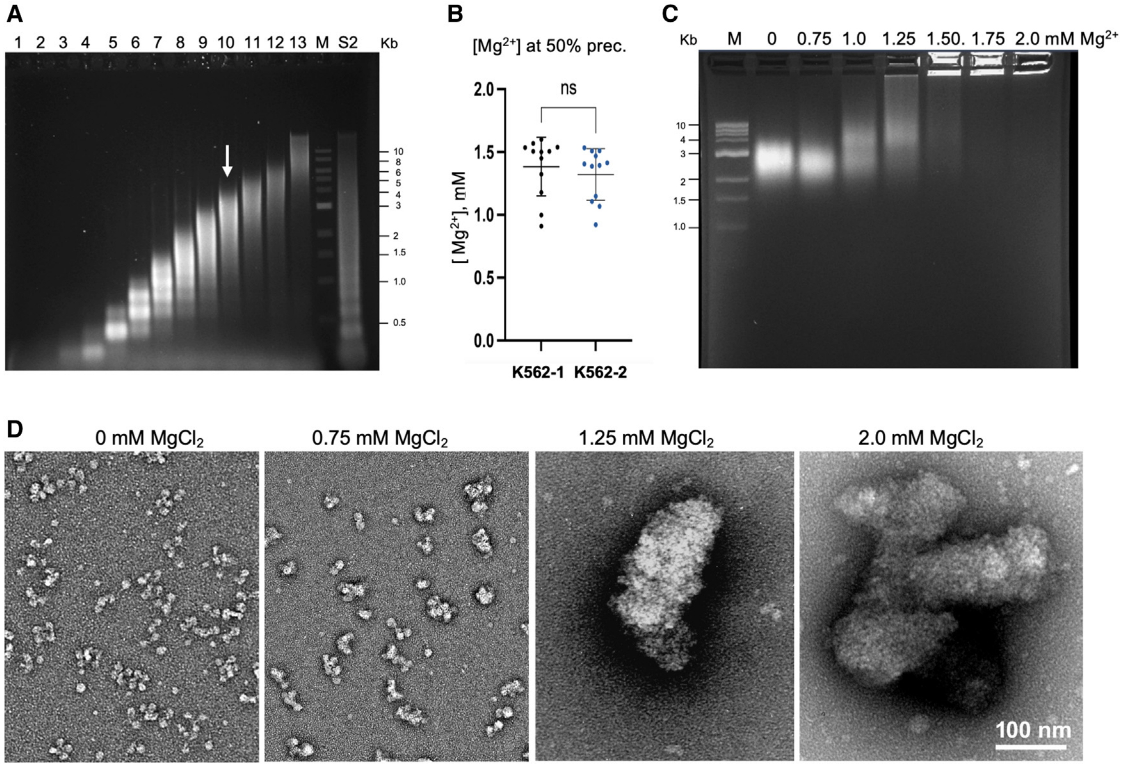

Figure 1. Biochemical and TEM characterization of Mg^{2+}-dependent secondary and tertiary structures in native human chromatin

(A) Agarose gel shows DNA of K562 chromatin fractionated by ultracentrifugation (lanes 1–13), DNA size markers (M), and unfractionated chromatin (S2). White arrow indicates fraction #10.

(B) 50% Mg^{2+}-precipitation points of chromatin fraction #10 from two independent batches of K562. Statistical significance: Student's t test.

(C) DNP agarose gel of chromatin crosslinked at the indicated concentrations of Mg^{2+}. M, DNA size markers.

(D) TEM of chromatin crosslinked at the indicated concentrations of Mg^{2+}. Scale bars, 100 nm.

secondary and tertiary structure may underlie the multiplex chromatin folding in living cells.

Cryoelectron tomography (cryo-ET) allows one to resolve biological structures embedded in thin layers of vitrified ice at nanoscale resolution.[39,40] Unlike the single-particle cryo-EM approach, which achieves angstrom-scale resolution by averaging images of many thousands of particles, cryo-ET can resolve individual molecules and molecular assemblies, which makes it ideal for multiplex nucleosome chain conformations. Cryo-ET was previously used to resolve nucleosome cores within cellular sections[41–44] as well as *in situ*-crosslinked and isolated chromatin,[45] although the nucleosome chain path and nucleosome interaction patterns have not been resolved. With isolated native interphase chromatin and metaphase chromosomes, the linker DNA can be resolved for long nucleosome arrays unfolded at relatively low ionic strength, showing a remarkable heterogeneity of linker DNA lengths.[13,46,47]

Here, we applied cryo-ET and nanoscale stereological modeling to trace individual nucleosomes within condensed human chromatin, where we observed abundant but non-uniform nucleosome stacking in *cis* and anti-parallel nucleosome interaction in *trans*, consistent with partial nucleosome interdigitation. We have shown that histone citrullination by protein arginine deiminase 4 (PAD4), which causes massive chromatin unfolding during NETosis[48,49] and contributes to deep vein thrombosis,[50] cancer metastasis,[51] and COVID-19 pathology,[52,53] causes a dramatic unfolding of the secondary and tertiary higher-order structures by disrupting the nucleosome stacking. We propose that the observed secondary structural features and linker DNA variability specific for native chromatin can explain its folding into discrete nanoparticles, in contrast to the extended zigzag 30-nm fiber in the reconstituted nucleosome arrays.

RESULTS

Cryo-ET reveals secondary and tertiary structures in Mg^{2+}-condensed human chromatin

We isolated micrococcal nuclease (MNase)-fragmented soluble chromatin from human K562 cells and fractionated chromatin by sucrose gradient ultracentrifugation to select a fraction containing ∼12 nucleosomes per particle (Figure 1A). We induced chromatin condensation by the divalent cation, Mg^{2+}, which causes compaction of nucleosome arrays at concentrations 0.5–1 mM[15,18] which is within the physiological range of free Mg^{2+} *in vivo*.[54] Upon increased Mg^{2+}, chromatin fractions showed a sharp self-association around 1.4 mM (Figures 1B and 1C), consistent with previous observations.[29,55] The chromatin samples were examined by transmission electron microscopy (TEM),

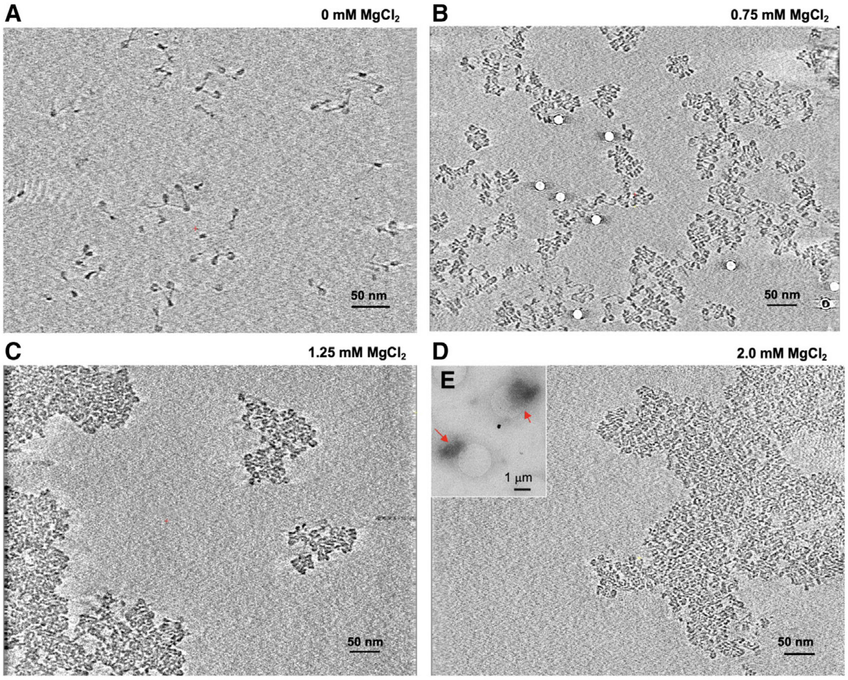

Figure 2. Cryo-ET reveals abundant nucleosome stacking within the secondary and tertiary chromatin structures

(A–D) Representative Z slices from cryotomograms of K562 chromatin vitrified without Mg^{2+} (A, TS_2_2), and with 0.75 mM (B, TS_4_4), 1.25 mM (C, TS_6_1), and 2.0 mM Mg^{2+} (D, TS_8_2). Mag: 53,000-x; scale bars, 50 nm.

(E) A portion of direct cryo-EM image (search mode) of K562 chromatin vitrified at 2.0 mM Mg^{2+}. Mag: 2,250-x; scale bar, 1 μm.

showing individual condensed arrays at 0.75 mM Mg^{2+} and bulky condensates at 1.25 and 2.0 mM Mg^{2+} (Figure 1D).

We then used cryo-ET and 3D reconstruction using IMOD[56] software to examine native chromatin particles vitrified with and without Mg^{2+} (Figure 2). Without Mg^{2+}, we observed unfolded nucleosome chains (Figure 2A) typical of open native chromatin.[13,46] In the presence of 0.75 mM Mg^{2+}, we found flat ladder-like nucleosome assemblies (Figure 2B) resembling those observed with reconstituted nucleosome arrays condensed by Mg^{2+}.[18] We did not observe either helical zigzag fibers[17] or columnar structures.[19] Native chromatin vitrified at 1.25 and 2 mM Mg^{2+} showed bulky tertiary structures (Figures 2C and 2D) with diameters exceeding 1 μm (Figure 2E). All cryotomograms are listed in Table S1.

Although we routinely used 20-min periods of Mg^{2+} incubation, in control experiments (Figure S1), we observed no signs of histone degradation during 48 h of incubation. Also, to avoid damage at the air/water interface,[57] we have examined the nucleosome integrity at the ice edges so that any damaged particles (yellow arrows) were excluded from the subsequent analysis. We also found no differences in Mg^{2+}-dependent self-association and chromatin folding for K562 cells blocked either in G1-phase or in S-phase (Figure S2). Furthermore, since the nucleosome repeat length (NRL) affects both secondary[58] and tertiary structures,[30] we analyzed chromatin from two other vertebrate cell types—human HeLa cells with an open euchromatin[33] and mouse retina cells that have exited the cell cycle and acquired condensed heterochromatin.[59] By MNase digestion, we measured the NRL in HeLa (184 bp) to be shorter than that in K562 (190 bp) and mouse retina (194 bp). However, by Mg^{2+} self-association and cryo-ET, all three cell types underwent very similar compaction with heterogeneous nucleosome stacking (Figure S2). We concluded that the major effect of physiological Mg^{2+} on chromatin structure is to promote the stacking of nucleosome disks and that the secondary and tertiary structures of condensed native chromatin are universal and independent of the cell cycle.

Cryo-ET reveals a wide variation in nucleosome linker lengths and plane orientations

To aid 3D visualization of chromatin particles, we processed the tomograms using deep-learning-based regression models trained in the Dragonfly Software suite using simulated cryo-ET data from cryo-TomoSim software.[60] This technique generates nearly noiseless tomograms, allowing the ready visualization of whole images and individual nucleosome arrays in 3D (Figure 3A; Videos S1 and S2). However, the deep-denoising technique occasionally flattened some low-signal regions. In comparison, on the unbinned simultaneous iterative reconstruction technique (SIRT)-reconstructed images, we could better resolve these structures, including thinner threads with lengths expected for the N-terminal tail of histone H3 and C-terminal tail of linker histone, and bulkier protrusions emanating from the nucleosome cores (Figure 3B, red and white arrows).

For quantitative stereological analysis, we used UCSF Chimera[61] to build nucleosome chain models by fitting PDB models of the nucleosome core (PDB: 2CV5[62]) into the tomographic density maps. The centroid and plane of each nucleosome were calculated, and centroids were connected into a chain by axes (Figure 3C) to form a centroid/axis/plane (CAP) model for each nucleosomal array. Snapshots of individual CAP models are shown in Figure S3. All CAP measurements are included in Table S2.

To perform stereological analysis, we modified the earlier two-angle chromatin model[22] and recorded five values for each nucleosome: (1) the center-to-center distance D from the next nucleosome in the chain, (2) the center-to-center distance N from the nearest nucleosome in 3D space, (3) the angle α between the two axes connecting each set of three consecutive nucleosomes in a chain, (4) the angle β between the planes of consecutive nucleosome pairs, and (5) the angle *para* between the planes of each nucleosome and its nearest neighbor in 3D space (Figure 3C; Video S3). Comparison between two independent batches of K562 cells showed a strong similarity between the nucleosome folding parameters (Figure S5).

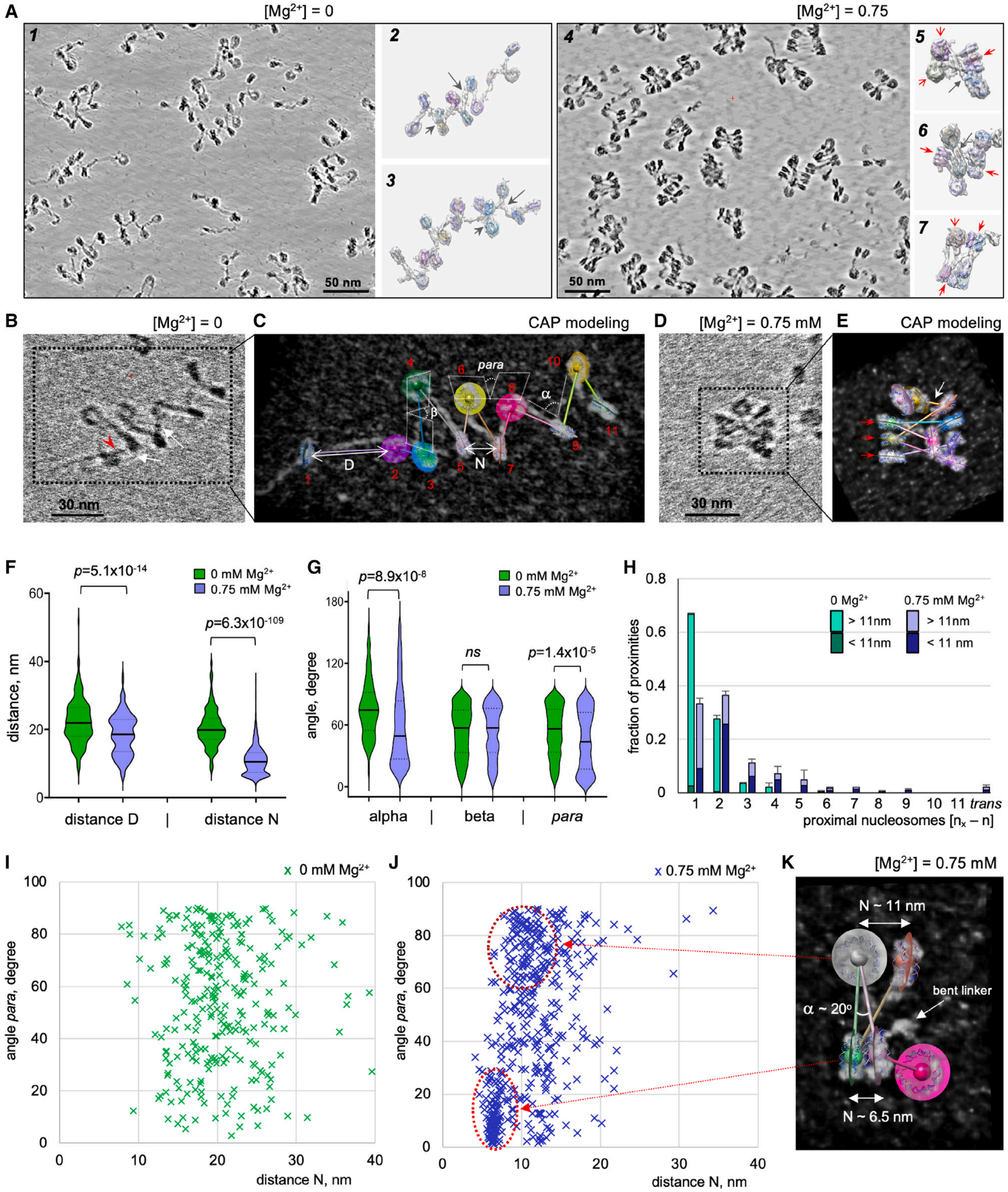

Figure 3. Cryo-ET and stereological modeling reveal individual variations of nucleosome spacing, orientation, and stacking in native chromatin

(A) Cryotomograms of K562 chromatin vitrified at 0 mM Mg^{2+} (A1–A3, TS_21_1, Video S1) and 0.75 mM Mg^{2+} (A4–A7, TS_22_1, Video S2) were processed by deep-learning denoising and shown as a composite of Z slices in IMOD (A1 and A4) and as individual particles transferred to chimera, volume-fitted with

(legend continued on next page)

In comparison with earlier estimations of linker DNA length variations of ±2 to ±4 bp,[63,64] we observed a wide distribution of distance D (Figure 3F) with standard deviation (SD) = ±6 nm corresponding to linker DNA variation of about ±20 bp (ca. 0.34 nm per DNA base pair). Short (~15–25 bp) and long (~70–80 bp) linkers were simultaneously present in the same arrays (Figure 3A). We confirmed this wide variation by tracing the open DNA regions between consecutive nucleosomes (Figure S4). The measured DNA linker lengths (L) showed a strong correlation with distance D and a similarly wide variation (45.0 ± 19 bp). Remarkably, the resulting average NRL (146 + 45 = 191 bp) is very close to the one observed by MNase digestion of K562 chromatin (190 ± 2 bp), despite the dramatically higher standard deviations.

The wide NRL variation is consistent with genome-wide mapping of nucleosome phasing[65] and cryo-ET analysis.[47] Still, being concerned whether our irregular nucleosome spacings could result from a positional reorganization upon isolation, we crosslinked K562 chromatin *in situ* and analyzed nucleosome distribution by cryo-ET and CAP modeling (Figure S4). The crosslinked samples displayed a highly significant reduction ($p < 10^{-8}$) in the average distance N and a strong increase in the internucleosomal contacts due to crosslinking. However, distance D displayed a similarly wide distribution in the crosslinked samples, consistent with the wide linker length variation.

Native chromatin folds into small clusters of stacked nucleosomes that do not form a progressive fiber

To further examine the internal organization of condensed native chromatin, we collected tomograms for 0.75 mM Mg^{2+}-condensed chromatin fractions (Figure 1A) and processed them by deep regressive denoising. The individual nucleosomes were best resolved for the smaller arrays (fraction 8), showing characteristic left-handedness of core DNA and linkers entering and exiting at close proximity (Figure 3A; Video S2). Remarkably, the nucleosomes were not stacked along one axis, such as observed with reconstituted nucleosomes,[17,18] but rather formed short stacks in various orientations. Most of the linkers were extended but did not fold congruently like steps of a spiral stair or flat ladder and often crossed each other at close distance (black arrows on panels 5 and 6). Some of the DNA linkers were bent (Figures 3E and 3K), consistent with the heteromorphic zigzag model,[33,66] but not with the solenoidal model.[67]

For quantitative stereological analysis of Mg^{2+}-condensed chromatin (Figure 3E; Video S4) and all other types of chromatin in this study, we used SIRT-reconstructed tomograms of chromatin from fraction 10 (~11 nucleosomes per array). We selected only free arrays or those that had no more than a single nucleosome contact with other particles and contained between 6 and 18 nucleosomes (Table S2).

Stereological comparison of chromatin at 0 and 0.75 mM Mg^{2+} (Figures 3F and S5) showed that the average distance D was reduced rather modestly, from 22.4 to 18.4 nm, consistent with partial linker DNA bending by Mg^{2+}. In comparison, the average distance N was reduced dramatically, from 20.4 to 10.9 nm, producing a sharp peak at 6–7 nm and a broader peak at 9–12 nm that correspond to parallelly stacked nucleosomes and perpendicularly juxtaposed nucleosome disks, respectively (Figure 3K). In condensed chromatin, angle α showed a highly significant difference ($p < 10^{-33}$) with a prominent peak at ~20°, whereas angle β did not change significantly. Angle *para* also displayed the most significant change ($p < 10^{-24}$) at values below 20° with a broad peak at ~10° in Mg^{2+}-condensed chromatin consistent with nucleosome stacking. Two-dimensional plotting of angles *para* vs. distance N reveals two distinct areas at 0.75 mM Mg^{2+} that are absent at 0 mM Mg^{2+} (Figures 3I and 3J). One is below 25° and centered at the distance N < 8 nm, corresponding to nucleosome stacking. 34.3% of all nucleosomes were stacked at 0.75 mM Mg^{2+} (no stacking occurred without Mg^{2+}). The other, more dispersed, range at 60°–90° angle *para*, is centered at the distance N ~ 11 nm and corresponds to near-perpendicular orientations of nucleosome disks. 35.4% of all nucleosomes fall into this category. The distribution of stacked nucleosomes per individual array at 0.75 mM Mg^{2+} varies widely, from 0% to 100%, and in most (63.6%) nucleosome arrays, the parallel stacking is interspersed with nucleosomes juxtaposed almost perpendicularly (Figure S5S).

Finally, we measured the nucleosome pairwise proximities between each nucleosome in the chain (n) and its closest counterpart in 3D (n_x). In the condensed chromatin, it was difficult to trace all linker DNAs; hence, only 78.6% of the distances D were recorded. When at least one distance D between nucleosomes n and n_x was missing, the interaction was not counted, so we recorded proximities for 65.6% of all nucleosomes. We compared the distance N and angle *para* for all nucleosomes and those with recorded D (D^+) and proximities (n_x^+) and found

nucleosome core structures, and shown as isosurfaces (A2, A3, and A5–A7). Short and long black arrows indicate short and long DNA linkers. Red arrows indicate nucleosome stacking perpendicular to (solid arrowheads) and along (open arrowheads) the viewer's z axis.

(B) Cropped cryotomogram of K562 chromatin at 0 mM Mg^{2+} (TS_1_1). Unidentified electron densities are indicated by white arrows (thin threads) and red arrowhead (bulky extranucleosomal protrusion).

(C) CAP model (1_1, Video S3) based on image (B). The scheme shows measured distances D and N and angles α, β, and *para*.

(D) Cropped cryotomogram of K562 chromatin vitrified at 0.75 mM Mg^{2+} (TS_4_1).

(E) CAP model (4_1, Video S4) based on image (D). Red arrows indicate nucleosome stacking direction perpendicular to the z axis, and white arrow indicates bent linker DNA.

(F and G) Violin plots of distances D and N (F), and angles α, β, and *para* (G) obtained for chromatin vitrified at 0 mM Mg^{2+} (green, n = 255 [D], 268 [N], 219 [α], 255 [β], 268 [*para*]), and at 0.75 mM Mg^{2+} (violet, n = 385 [D], 457 [N], 293 [α], 363 [β], and 457 [*para*]). Statistical significance: Student's t test.

(H) Distribution of nucleosome proximities in chromatin vitrified at 0 mM Mg^{2+} (green columns, n = 267) and at 0.75 mM Mg^{2+} (violet columns, n = 305). Darker and lighter colors designate proximities at <11 nm and >11 nm, respectively. Error bars: SD values calculated for the total datasets.

(I and J) Two-dimensional plots of the angle *para* vs. distance N for chromatin vitrified at 0 mM Mg^{2+} (I) and 0.75 mM Mg^{2+} (J).

(K) CAP model (3_20, Video S5) based on cropped cryotomogram of chromatin at 0.75 mM Mg^{2+} (TS_3_1). Angle α distances N between selected nucleosome pairs and one bent linker DNA are indicated.

no significant differences (Figures S5P and S5Q), indicating an absence of nonrandom bias.

Figure 3H shows pairwise proximities between total nucleosomes and those juxtaposed at N < 11 nm, i.e., likely to be in direct contact.[33] The Mg^{2+}-condensed chromatin showed a strong decrease in the overall nucleosome proximities at i ± 1 together with a profound increase in i ± 1, i ± 2, i ± 3, i ± 4, and i ± 5 proximities with N < 11 nm. The i ± 2 dominates in the condensed chromatin, which is strikingly similar to the observations by *in situ* EM-assisted nucleosome interaction capture (EMANIC)[33] (Figure S5T) and consistent with the genome-wide nucleosome interaction mapping in other mammalian cells.[34–36] We thus concluded that the overall secondary structure of native chromatin incorporates a multitude of linker DNA lengths and conformations that deviate from either the progressive zigzag folding or columnar structures observed in the reconstituted nucleosome arrays but are remarkably similar to those observed *in situ*.

Chromatin condensates retain small clusters of nucleosome stacking

Although for analysis of the secondary chromatin structures, we focused on separate nucleosome arrays, even at 0.75 mM Mg^{2+}, some arrays formed larger self-associated particles (Figures 4A1–4A6). Remarkably, in addition to the nucleosome stacking with parallel-oriented dyad axes, some nucleosomes within the self-associated arrays were either stacked in an anti-parallel orientation or were only partially overlapping (red arrows).

At 1.0 mM Mg^{2+}, nucleosome arrays formed bulky tertiary structures intermixed with detached nucleosome arrays (Figures 4A7–4A9). At the edges, the nucleosomes were self-associated two-dimensionally and could be resolved by cryo-ET for CAP modeling, showing that some nucleosome disks were engaged in anti-parallel stacking (red arrows). Such nucleosome arrangement is consistent with earlier nucleosome interdigitation models proposed for heterochromatin[68] and metaphase chromosomes.[69] However, in the Mg^{2+}-condensed total chromatin, the interdigitation involved small clusters of 2–4 nucleosomes and did not spread globally.

At Mg^{2+} concentrations exceeding 1 mM, nucleosome arrays formed bulky condensates larger than 100 nm that were confined to 50–80-nm thick slabs of the vitrified ice, facilitating their imaging by cryo-ET (Figures 4A10–4A12). Nucleosomes within the condensed chromatin particles showed distinct patterns of "mud-brick layering" apparent on the side projections (Figure S6). Our denoising methods did not yield clearly distinguishable nucleosomes in the middle of these condensates, but we could resolve clusters of condensed nucleosomes near the edge.

Stereological comparison of chromatin vitrified at 1.25 and 0.75 mM Mg^{2+} (Figures 4B–4F) showed no significant difference in distance N distribution. At 1.25 mM Mg^{2+}, the angle *para* showed a notable decrease above 70°. However, the clustered area corresponding to the tightly stacked nucleosome disks (<25° *para*, N $\sim$ 6.5 nm) remained pronounced at 1.25 mM Mg^{2+}. Thus, in contrast to the previous lower-resolution imaging suggesting the fully disordered nature of nucleosome condensates,[29–31] our cryo-EM images showed a clear retention of partial nucleosome stacking in the Mg^{2+}-induced tertiary chromatin structure, although the nucleosome stacks are small and do not spread globally within the condensed chromatin.

PAD4-dependent histone citrullination inhibits nucleosome stacking and chromatin folding at the secondary and tertiary levels

Chromatin higher-order folding is subject to regulation by post-translational histone charge modification.[70,71] One of the strongest effects on global chromatin folding is imposed by histone arginine citrullination catalyzed by arginine deiminase PAD4, which mediates the formation of neutrophil extracellular traps or NETs.[48,49] Because chromatin from human neutrophils undergoes extensive histone proteolysis, here, we employed chromatin from K562 cells that are derived from immature precursors of neutrophils, do not express the granule proteases, and display chromatin epigenetic marks similar to those of mature neutrophils.[72]

We treated native chromatin with PAD4 in the presence of $CaCl_2$ (PAD4 co-enzyme). The PAD4-treated and control chromatin samples were analyzed electrophoretically (Figure 5A) to monitor histone citrullination by the downward mobility shifts of histone H3 and H4, due to the positive charge reduction resulting from citrullination at histone H3 Arg8 and Arg17 and histone H4 Arg3.[73] The sodium dodecyl sulfate-polyacrylamide gel electrophoresis (SDS-PAGE) gel shows a complete shift of histones H3 and H4 in PAD4-treated but not control chromatin, indicating that the chromatin modification is fully dependent on PAD4 and not due to chromatin degradation. We confirmed this result by western blotting with antibodies against citrullinated histone H3 (Abcam ab5103) and by Triton-acetate-urea gels,[74] showing the upward shifts of histone H4 and H3 variants resulting from positive charge reduction consistent with the extent of histone H3 and H4 citrullination by PAD4.[73] We then monitored the effect of PAD4 citrullination on chromatin folding by deoxyribonucleoprotein (DNP) agarose gel and Mg^{2+}-dependent self-association (Figures 5B and 5C) and observed a prominent inhibition of chromatin folding by PAD4.

Cryo-ET of the control and PAD4-treated chromatin (Figures 5D and S6) showed no substantial difference in nucleosome folding at 0 mM Mg^{2+}. In the presence of 0.75 mM Mg^{2+}, however, the control chromatin showed a higher extent of compaction and stacking. At 1.0 mM Mg^{2+}, the control-treated chromatin displayed self-association, whereas the PAD4-treated arrays remained dissociated, showing that the formation of compact chromatin structures is significantly inhibited by histone citrullination.

CAP modeling and stereological analysis (Figures 5E–5H and S7) showed no significant differences at 0 mM Mg^{2+}. At 0.75 mM Mg^{2+}, distance D and angle β were not significantly affected. In contrast, the average distance N was significantly ($p < 10^{-8}$) increased, from 10.7 to 13.1 nm in PAD4-treated samples, with a sharp decrease in the peak corresponding to nucleosome stacking (6.5 nm). The angle α distribution showed a significant decrease below 20° ($p < 10^{-6}$), consistent with histone citrullination mainly affecting closely juxtaposed linkers. For angle *para*, the most significant difference ($p < 10^{-8}$) was also observed for the lowest 20%. The two-dimensional plots (Figures 5G and 5H) revealed the strongest change in the area

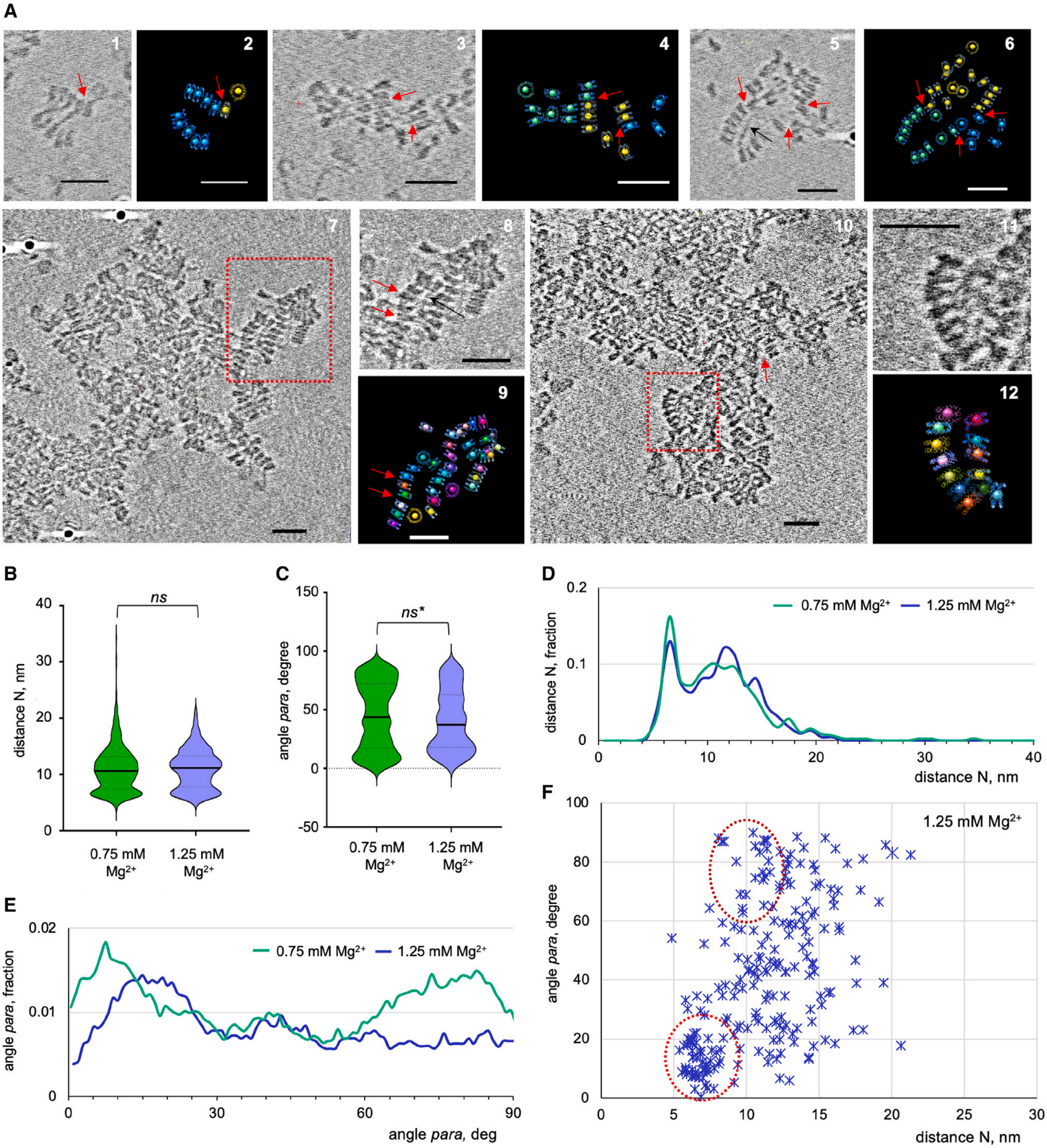

Figure 4. Cryo-ET and 3D modeling reveal *cis*- and *trans*-internucleosomal stacking within the self-associated native nucleosome arrays

(A) (A1, A3, and A5) Cropped cryotomograms showing K562 arrays vitrified at 0.75 mM Mg^{2+} and connected in-*trans*: TS_3_3 (A1 and A3) and TS_3_2 (A5). (A2, A4, and A6) CAP models 3_16, 3_21, and 3_22 based on images in (A1), (A3), and (A5), respectively. (A7–A12) Cryotomograms TS_5_1 (A7) and TS_6_2 (A10), cropped images (A8 and A11), and associated CAP model 5_1 (A9) and 6_2_1 (A12) of chromatin vitrified at 1.0 mM Mg^{2+} (A7–A9) and 1.25 mM Mg^{2+} (A10–A12). Red arrows show nucleosome disks stacked in an anti-parallel orientation or partially overlapping. Black arrow shows linker DNA crossing the plane of nucleosome stacking. Scale bars, 30 nm.

(B–E) Violin plots (B and C) and frequency distribution profiles (D and E) of distances N (B and D), and angle *para* (C and E) of chromatin vitrified at 0.75 mM Mg^{2+} (green, n = 457) and 1.25 mM Mg^{2+} (violet, n = 223). Statistical significance: Student's t test (*p = 0.01 by Kolmogorov-Smirnov test).

(F) Two-dimensional plot of the angle *para* vs. distance N for the nucleosomes vitrified at 1.25 mM Mg^{2+}.

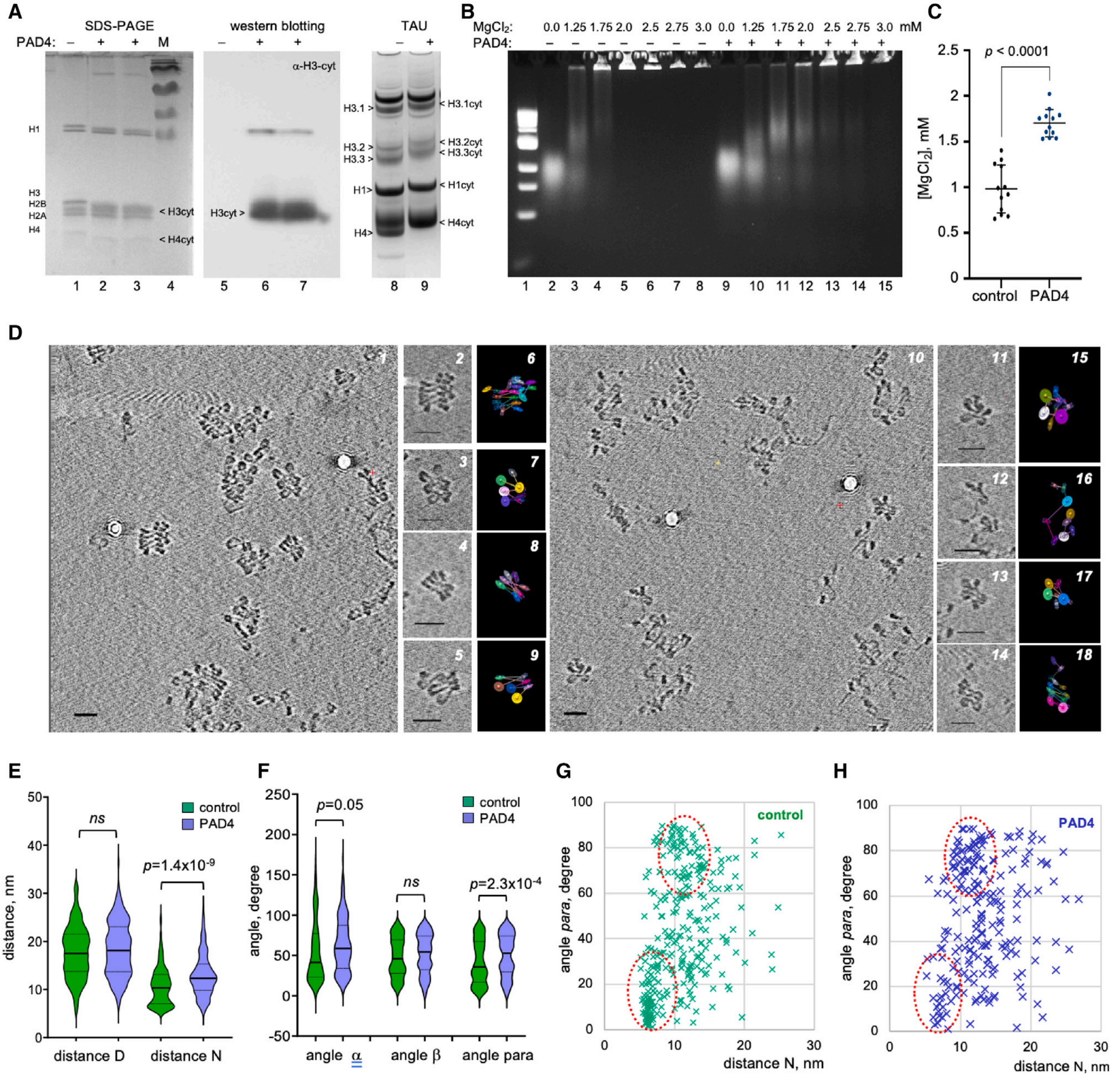

Figure 5. Inhibition of native chromatin higher-order folding by PAD4-dependent histone citrullination

(A) Lanes (A1–A3) 18% SDS-PAGE shows histones of control (A1) and PAD4-treated (A2 and A3) K562 chromatin. Lane (A4): m.w. markers. Lanes (A5–A7) 8%–16% gradient SDS-PAGE of histones from control (A5) and PAD4-treated (A6 and A7) chromatin followed by western blotting detected by antibodies against citrullinated histone H3. Lanes (A8 and A9) Triton-acetate-urea gel shows histones from control (A8) and PAD4-treated (A9) chromatin.

(B) DNP agarose gel showing DNA size markers (lane B1) and native electrophoresis of control (lanes B2–B8) and PAD4-treated (lanes B9–B15) chromatin.

(C) 50% Mg^{2+}-precipitation points determined for control and PAD4-treated chromatin. Statistical significance: Student's t test.

(D) (D1–D9) Cryotomogram TS_14_2 (D1), cropped images (D2–D5), and CAP models 14_7 (D6), 14_8 (D7), 14_10 (D8), and 14_6 (D9) based on images (D2)–(D5) showing control chromatin vitrified at 0.75 mM Mg^{2+}. (D10–D18) Cryotomogram TS_16_1 (D10), cropped images, and CAP models 16_8 (D15), 16_10 (D16), 16_11 (D17), 16_1 (D18). Showing PAD4-treated chromatin vitrified at 0.75 mM Mg^{2+}. Scale bars, 30 nm.

(E and F) Violin plots of distances D and N (E) and angles α, β, and *para* of control (green) and PAD4-treated (violet) chromatin. Control samples: n = 209 (D), n = 302 (N), n = 162 (α), n = 209 (β), and n = 302 (*para*); PAD4-treated samples: n = 162 (D), n = 215 (N), n = 130 (α), n = 162 (β), and n = 215 (*para*). Statistical significance: Student's t test.

(G and H) Two-dimensional plots of angle *para* vs. distance N for control (G) and PAD4-treated (H) chromatin.

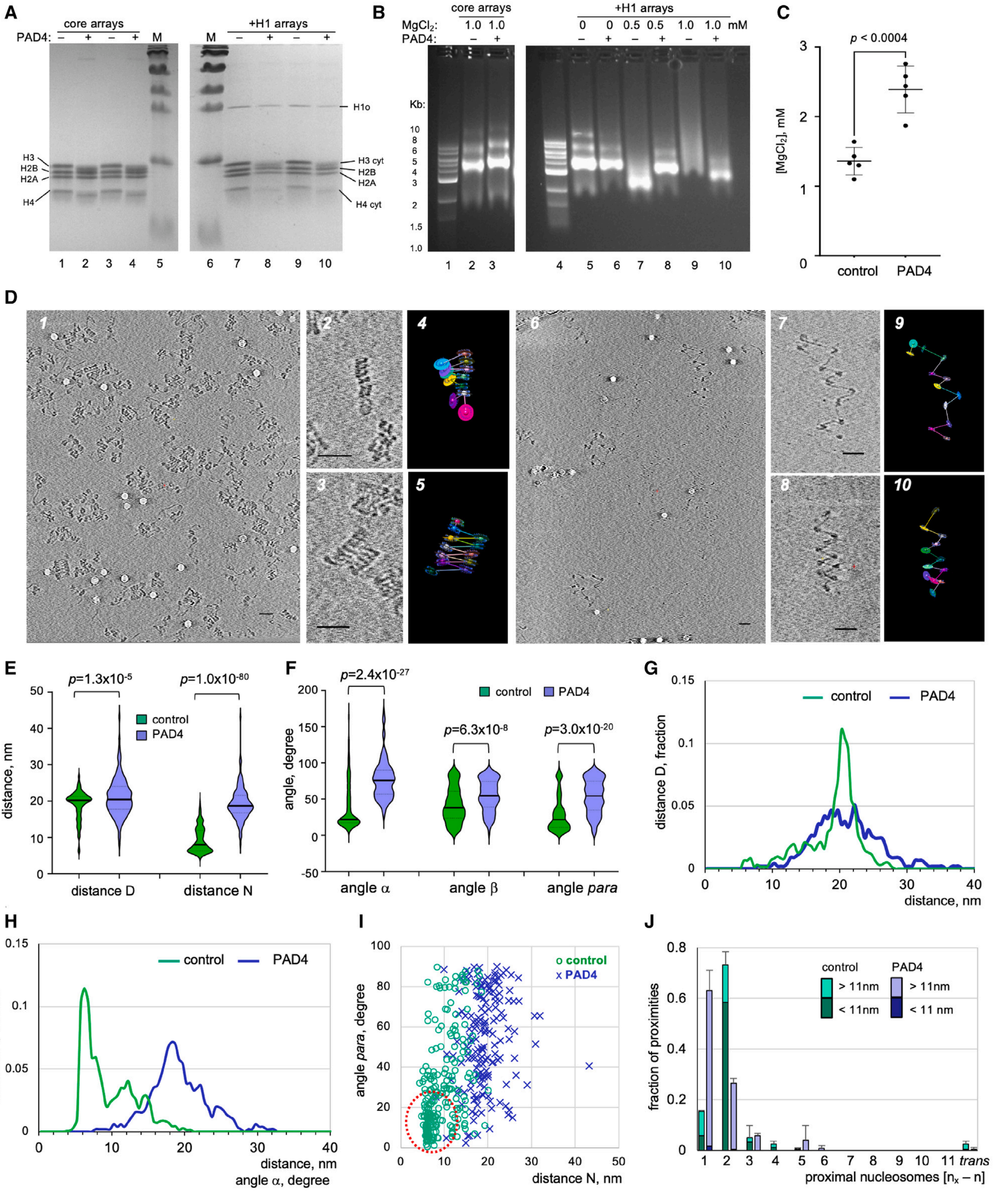

Figure 6. Nucleosome chain folding in clone 601-based reconstituted nucleosome arrays and its inhibition by histone citrullination

(A) Lanes (A1–A5): 18% SDS-PAGE shows histones of control (A1 and A3) and PAD4-treated (A2 and A4) reconstituted 183 × 12 arrays. M, m.w. markers. Lanes (A6–A10): 18% SDS-PAGE shows histones of control (lanes A7 and A9) and PAD4-treated (A8 and A10) 183 × 12 + H1 arrays.

(legend continued on next page)

corresponding to the tightly stacked nucleosome disks (<25° *para*, N ~ 6.5 nm). Unlike chromatin unfolding at low salt (Figure 3J), PAD4 treatment did not reduce the area corresponding to perpendicular nucleosome disks (60°–90° *para*, N ~ 8–12 nm). Thus, we concluded that PAD4-induced histone citrullination was specifically inhibiting nucleosome stacking, although it had a relatively little effect on the conformation of nucleosome linkers or the spatial organization of the non-stacked nucleosomes in native chromatin.

Reconstituted nucleosome arrays are dramatically unfolded by histone citrullination

The partial unfolding of native chromatin by histone citrullination notably differed from the almost complete unfolding observed for reconstituted arrays.[48] We reasoned that because histone citrullination mostly targets nucleosome disk stacking, its effect would be stronger for reconstituted arrays with uniform nucleosome stacking.[18] Therefore, we constructed 12-nucleosome arrays based on clone 601 with NRL of 183 bp, as previously described.[33,75] This NRL is a representative of the 10n + 5 class of nucleosome linkers (~172, 183, and 193 bp), typical of natural chromatin.[76]

The 183 × 12 nucleosome arrays were treated with PAD4 and analyzed by 18% SDS-PAGE to confirm a complete shift of histones H3 and H4 (Figure 6A). The PAD4-treated and control arrays were then mixed with recombinant linker histone H1° as described,[33] at a ratio of 0.7 molecules per nucleosome, which is close to natural stoichiometry of histone H1.[77] We reconstituted linker histone H1 with the already citrullinated nucleosome arrays because PAD4 partially citrullinates histone H1 (Figure 5A), and we sought to study the effect of core histone citrullination.

By DNP agarose electrophoresis and Mg^{2+} self-association (Figures 6B and 6C), we observed that a strong downward shift in control H1-reconstitued arrays at 0.5 mM Mg^{2+} and a prominent band smearing at 1 mM Mg^{2+} were both almost completely inhibited by PAD4 treatment. In parallel, there was a strong change in Mg^{2+}-dependent self-association. Thus, PAD4-mediated histone citrullination had a profound inhibitory effect on the secondary and tertiary chromatin structures of linker histone-reconstituted nucleosome arrays.

Cryo-ET of control and PAD4-treated 183 × 12 + H1 arrays (Figure 6D) showed a dramatic effect of PAD4 treatment, resulting in complete unfolding into extended zigzag chains in full agreement with the solution assays above. CAP modeling and stereological analysis of control and PAD4-treated 183 × 12 + H1 arrays (Figures 6E–6J and S7) showed that the average distance N increased more than 2-fold, from 9.3 to 19.3 nm ($p < 10^{-80}$), dramatically stronger than that in the PAD4-treated native chromatin. This leads to a complete disappearance of the "nucleosome stacking" peak at 6.5 nm. In PAD4-treated arrays, distance D distribution showed a striking loss of the sharp peak centered at 21 nm, and angle α showed an equally dramatic loss of its major peak at ~18°. Similarly, angles β and *para* both showed significant changes resulting from histone citrullination. A two-dimensional plot of *para* vs. N reveals an obvious change in the area below 30° angle *para* and distance N ~ 6.5 nm (dashed oval). Accordingly, the peak of nucleosome proximities at i ± 2 was dramatically reduced by PAD4 treatment in parallel to an equally strong increase in i ± 1, which corresponds to an extended nucleosome chain (Figure 6J). Thus, the reconstituted nucleosome arrays showed a dramatic unfolding by PAD4-mediated histone citrullination, exceeding that in the native chromatin and consistent with complete disruption of the overall nucleosome disk stacking in reconstituted clone 601-based arrays.

Nanoscale spatial analysis reveals fundamental topological differences between the native and reconstituted nucleosome array folding

Since most previous chromatin structural studies have focused separately on either native[10–12] or reconstituted chromatin,[14–18] here, we used cryo-ET to compare the 3D structures of both types condensed by 0.75 mM Mg^{2+} (Figure 7). Distance D distribution showed a striking contrast between one sharp peak at 21 nm in the reconstitutes and several broad peaks in the native chromatin, fully consistent with the uniform DNA linker lengths in the former and the wide variability in the latter. Compared with reconstituted arrays, distance N in native chromatin showed a notably higher broad peak at ~8–14 nm, corresponding to neighboring nucleosome disks at a perpendicular orientation. The angle α distribution displayed a much higher and narrower peak at ~18° in the reconstituted arrays, whereas the values between 60° and 100° were higher in native chromatin. Notably, this range of angles α may reflect the presence of unfolded linker DNA in the Mg^{2+}-condensed native chromatin originating from

---

(B) DNP agarose gels showing DNA size markers (lanes B1 and B4) and native electrophoresis of the control (lane B2) and PAD4-treated (lane B3) 183 × 12 arrays crosslinked at 1 mM Mg^{2+} and control (lanes B5, B7, and B9) and PAD4-treated (lanes B6, B8, and B10) 183 × 12 + H1 arrays crosslinked at 0–1 mM Mg^{2+} as indicated.

(C) 50% Mg^{2+}-precipitation points of control and PAD4-treated 183 × 12 + H1 arrays. Statistical significance: Student's t test.

(D) (D1–D5) Cryotomogram TS_17_6 (D1), cropped images (D2 and D3), and associated CAP models 17_6 (D4) and 19_4 (D5) showing control 183 × 12 + H1 arrays vitrified at 0.75 mM Mg^{2+}. (D6–D10) Cryotomogram TS_18_3 (D6), cropped images (D7 and D8), and associated CAP models 18_1 (D9) and 18_7 (D10) showing PAD4-treated 183 × 12 + H1 arrays vitrified at 0.75 mM Mg^{2+}. Scale bars, 30 nm.

(E and F) Violin plots showing distribution of internucleosomal distances D and N (E) and angles α, β, and *para* (F) measured for control (green) and PAD4-treated (violet) 183 × 12 + H1 arrays at 0.75 mM Mg^{2+}. Statistical significance: Student's t test.

(G and H) Frequency distribution profiles of distances D (G), and N (H) measured for control (green) and PAD4-treated (violet) 183 × 12 + H1 arrays at 0.75 mM Mg^{2+}. Control samples: n = 204 (D), n = 230 (N), n = 197 (α), 217 (β), and 230 (*para*). PAD4-treated samples: n = 150 (D), n = 158 (N), n = 135 (α), n = 150 (β), and n = 158 (*para*).

(I) Two-dimensional plot showing angle *para* vs. distance N for control (green) and PAD4-treated (blue) 183 × 12 + H1 arrays at 0.75 mM Mg^{2+}.

(J) Nucleosome proximities determined for control (green) and PAD4-treated (violet) 183 × 12 + H1 arrays at 0.75 mM Mg^{2+}. Control samples: n = 237; PAD4-treated samples: n = 165. Darker and lighter colors designate proximities at <11 nm and >11 nm, respectively. Error bars: SD values calculated for the total datasets.

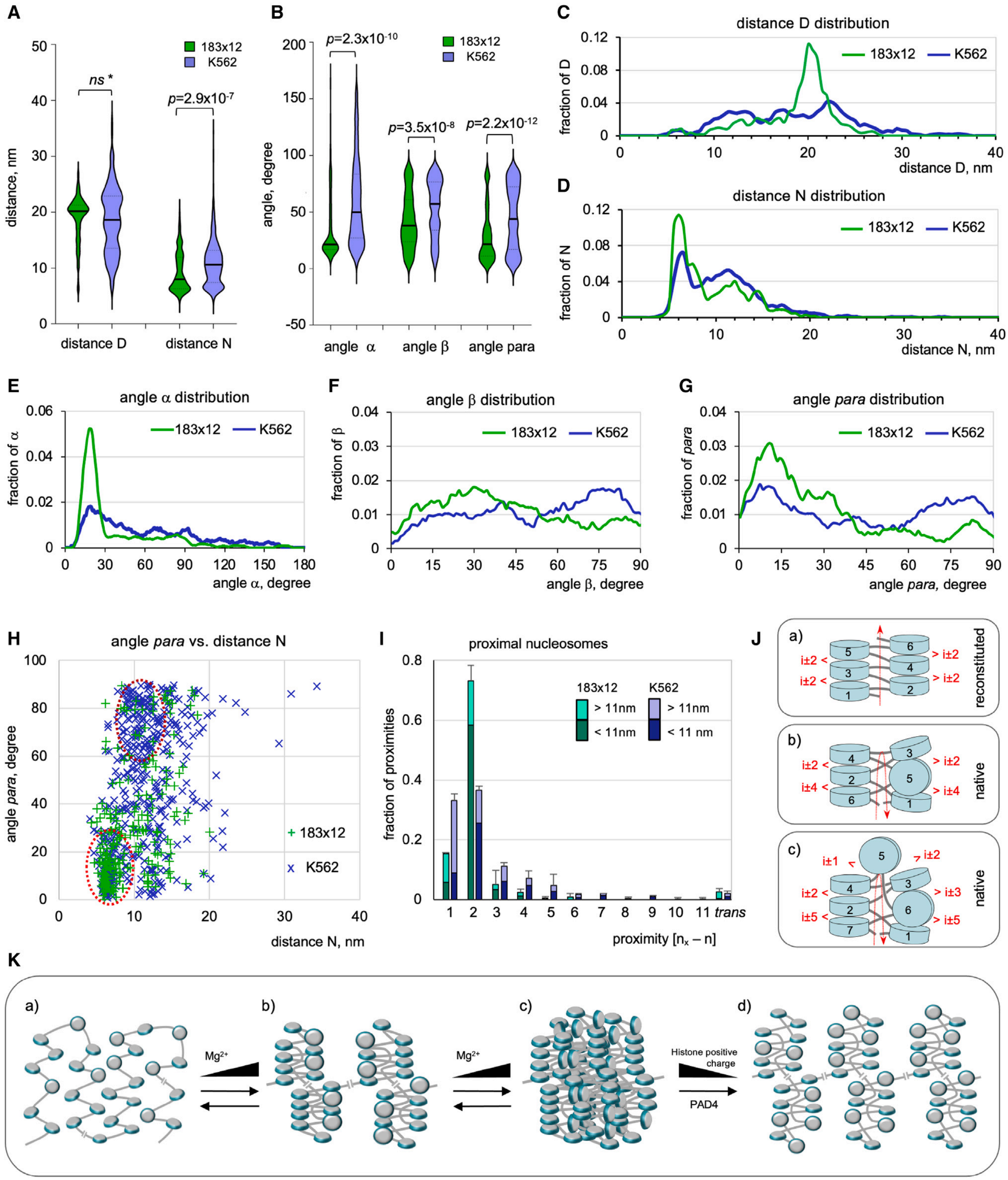

Figure 7. Comparative stereological analysis of the native and reconstituted chromatin folding

(A and B) Violin plots comparing distributions of distances D and N (A) and angles α, β, and *para* (B) of 183 × 12 + H1 arrays (green) and K562 chromatin (violet) at 0.75 mM Mg^{2+}. Statistical significance: Student's t test (*p = 3.3 × 10^{-5} by Kolmogorov-Smirnov test).

(C–G) Frequency distribution profiles comparing distances D (C), N (D), and angles α (E), β (F), and *para* (G) of 183 × 12 + H1 arrays (green) and K562 chromatin (blue) at 0.75 mM Mg^{2+}.

(legend continued on next page)

substoichiometric association with liker histone H1.[77] The largest difference in angle β was manifested by the notably diminished peak at 60°–90° in reconstituted arrays, which represents consecutive nucleosomes with planes oriented perpendicularly (e.g., nucleosomes #3 and #5 on Figures 7Jb).

The percentage of nucleosomes with high angle *para* (above 60°) was dramatically higher in the native chromatin (38.5%) than that in the reconstituted arrays (14.4%). On the two-dimensional plotting (Figure 7H), the clustered area corresponding to perpendicular nucleosome disks (60°–90° *para*, N ∼ 8–14 nm) is largely suppressed in the reconstituted nucleosome arrays, consistent with the absence of proximal nucleosomes with perpendicular nucleosome planes in the reconstituted arrays (Figure 6D).

The comparison of nucleosome interactions showed strong proximities at i ± 1, i ± 3, i ± 4, and i ± 5 in native chromatin that were virtually absent from the reconstituted arrays (Figure 7I). This trend was fully retained for the closely juxtaposed nucleosomes ($N < 11.0$ nm), suggesting a fundamental difference in interactions of the tightly packed nucleosomes. Upon revisiting the native nucleosome models and datasets (Figure S3; Table S2), we found that the i ± 1, i ± 3, i ± 4, and i ± 5 interactions originated from native nucleosome arrays deviating from the progressive zigzag path and, after making a U-turn, forming regressive zigzag folds with crisscrossed linker DNA (e.g., Figures 3A7 and 3K), bent linker DNA (Figure 3E), or long linkers crossing the axis of stacking (Figures 3A5 and 3A6). As schematically shown in Figure 7J, depending on the even or odd number of nucleosomes making the U-turn, such structures would either display even (i ± 2 and i ± 4, "native" cartoon b) or odd (i ± 1, i ± 3, and i ± 5, native cartoon c) proximities. In contrast, the reconstituted arrays, which form a classic two-start zigzag fiber, are expected to display only i ± 2 proximities ("reconstituted" cartoon a). Thus, the nanoscale spatial analysis of native chromatin folding revealed the following three novel features specific to the condensed native chromatin: (1) the discontinuous asymmetric nucleosome stacking, (2) the alternating parallel and perpendicular orientations of the juxtaposed nucleosome disks, and (3) regressive folding of nucleosome chains that, despite displaying prominent zigzag features, fold into discontinuous nanoparticles rather than continuous fibers.

DISCUSSION

Chromatin higher-order folding accommodates nucleosome chains with highly variable spacing

Our cryo-ET analysis reveals the regressive zigzag path of the nucleosome chain in native condensed chromatin. This finding helps to reconcile long-standing controversies regarding chromatin folding *in vitro* and in the interphase cell and provides novel mechanistic insights into the cooperation of distinct structural motifs in higher-order chromatin folding. In living cells, the nucleosomes may fold into small clutches or nanodomains[27,28,78] that undergo dramatic unfolding mediated by epigenetic mechanisms.[38,79] Here, we propose a general model for nucleosome chain folding into a discontinuous secondary structure composed of stacks of closely juxtaposed nucleosomes interrupted by nucleosomes oriented perpendicularly to their neighbors. Such structures incorporate both short and long DNA linkers and make sharp U turns, forming nanodomains with a regressive nucleosome chain path (Figure 7K). This multiplex secondary structure is fundamentally different from either regular zigzag fibers[17,18] or columnar structures[19] observed for reconstituted nucleosome arrays. However, it appears to be best suited to pack the native nucleosomes with highly variable spacing.[47,65] Our findings are also consistent with the high polymorphism of chromatin fibers with variable NRL predicted by Monte Carlo simulations.[80]

Surprisingly, the apparently irregular and weak nucleosome folding is not completely erased from the native chromatin by PAD4 (Figure 5), which completely unfolds reconstituted arrays (Figure 6). This raises the interesting possibility that the multiplex folding motifs generate local nucleosome chain topologies that are either more or less prone to unfold upon histone charge modifications and thus "remember" their repressed or active epigenetic states.

Either in crystal structures or in regular reconstituted arrays, the nucleosome disks tend to be fully engaged in close parallel stacking mediated by contacts between histone H4 N-terminal domains and the acidic patch of histone H2A/H2B dimer.[1,15] Nucleosome surfaces, including the acidic patch, interact with multiple chromatin regulatory and architectural factors.[81] The cooperative nucleosome stacking presents a major energetic barrier for chromatin unfolding and is strongly dependent on the linker DNA length,[82,83] which in living cells is dynamically regulated by ATP-dependent chromatin remodelers.[84] Whether nucleosome arrays with the maximal or minimal percentage of stacking originate from repressed or active chromatin domains and regions with specific nucleosome positioning requires further investigation.

Our cryo-ET analysis of nucleosome proximities in native chromatin (Figure 3H) showed a pattern consistent with the regressive chromatin zigzag path (Figure 7K) and, at the same time, was remarkably similar to *in situ* interaction mapping by radiation-induced cleavage of DNA,[34] Micro-C,[35,36] and EMANIC.[33] Furthermore, our cryo-ET imaging of discontinuous nucleosome stacks is consistent with the highly variable structures observed

---

(H) Two-dimensional plot of angle *para* vs. distance N for 183 × 12 + H1 arrays (green) and K562 chromatin (blue) at 0.75 mM Mg^{2+}.

(I) Nucleosome proximities determined for 183 × 12 + H1 arrays (green, n = 180) and K562 chromatin (violet, n = 305) at 0.75 mM Mg^{2+}. Darker and lighter colors designate nucleosome proximities at <11 nm and >11 nm, respectively. Error bars: SD values calculated for the total datasets.

(J) Cartoon models illustrating the paths of nucleosome chain folding in the reconstituted arrays (Ja) and two types of native nucleosome arrays (Jb and Jc). Dashed red arrows show directions of the zigzag fiber axes.

(K) Schematic models showing (Ka) chains of nucleosomes with heterogeneous linker lengths and plane orientations folding into (Kb) the secondary structure: nanoparticles mediated by nucleosome stacking in *cis* and (Kc) the tertiary structure: nanoparticles joined together by nucleosome stacking in-*cis* and in-*trans*. (Kd) Histone modifications reducing the net positive charge of the histones (such as histone citrullination) mediate a complete unfolding of the tertiary structure and partial unfolding of the secondary structure by disrupting the nucleosome stacking while preserving the local topologies of nucleosome chains.

by EM tomography of chromatin *in situ*.[25] We expect that our regression denoising algorithms,[60] combined with 3D visualization and CAP modeling, would be efficient tools for developing new 3D nucleosome chain models for computational reconstructions of chromatin structures observed *in situ*, e.g., in vitrified cellular sections.[41–44]

Role of Mg^{2+}-cations in nucleosome chain folding and self-association

Mg^{2+}-induced native chromatin folding and non-uniform nucleosome stacking occur at 0.5–0.75 mM Mg^{2+} (Figure 2), which is remarkably close to the physiological concentration of free Mg^{2+}, estimated at ~0.6 mM in the interphase cell.[54] Further increase in Mg^{2+} promotes metaphase chromosome condensation *in vivo*[54,85] by a process very similar to the Mg^{2+}-dependent self-association *in vitro*.[29] We thus assume that the Mg^{2+}-induced structural transitions of native chromatin observed by cryo-ET correctly reproduce those observed *in vivo* at similar Mg^{2+}-concentrations.

In addition to the uniform electrostatic screening of negative charges in DNA, Mg^{2+} has been shown to alter chromatin folding in a sequence-specific manner[86] and has been proposed to facilitate condensation of heterochromatin enriched by repetitive satellite DNA.[87] Further work on Mg^{2+}-induced compaction of fractionated heterochromatin, followed by cryo-ET and DNA sequencing, should reveal the nature of these genomic regions and chromatin states regulated by nucleosome stacking.

Previous TEM studies of large nucleosome condensates did not reveal any distinct structural elements, such as 30-nm fibers.[29] More recently, the mechanism of cation-dependent condensation and self-association of nucleosome arrays has been described as a liquid-liquid phase separation (LLPS), where the condensed nucleosome arrays reside in a fluid, unstructured state.[30] Despite this apparent fluidity, our cryo-ET showed multiple internucleosomal contacts mediated by anti-parallel stacking of nucleosome disks. Such contacts are consistent with the nucleosome interdigitation hypothesis previously proposed as a mechanism of global nucleosome condensation in heterochromatin[68] and metaphase chromosomes.[69] Unlike these idealized models, the anti-parallel nucleosome stacking observed by cryo-ET formed a minority of all visible interactions (Figure 4). We suggest that in the process of Mg^{2+}-mediated condensation, the nucleosome surfaces that remain open at the periphery of compact nanoparticles would interact in *trans* and form contacts between the anti-parallel nucleosome surfaces, leading to the formation of bulky nucleosome condensates (Figure 7K). Intriguingly, several nucleosome core crystal lattices display anti-parallel "head-to-tail" nucleosome stacking consistent with in *trans* nucleosome interactions.[68,88,89] It remains to be shown whether the nucleosomes that resist in-*cis* stacking in the secondary structure but are engaged in in-*trans* stacking in the tertiary structure bear any specific histone variants or other epigenetic marks regulating the process of global chromatin condensation.

Implications for NETosis

One of the strongest effects on global chromatin folding is imposed by histone arginine citrullination by PAD4, which causes massive chromatin unfolding during NETosis in neutrophil granulocytes.[48,49] During granulocyte maturation, the chromatin condenses and accumulates abundant tertiary structures[44] before acquiring the ability to release NETs.[90] We propose that a major effect of PAD4-induced citrullination is to reduce the tertiary chromatin structure by inhibiting nucleosome stacking interactions at physiological Mg^{2+} concentrations. This structural transition, although insufficient by itself to unfold the chromatin into NETs, may trigger NETosis by unfolding the nucleosome condensates and opening them to additional factors, such as calpain protease,[91] which would cause proteolysis of histones and other nuclear architectural proteins, leading to complete nuclear rupture.[92]

The fact that PAD4-mediated NETosis, despite its benefits for wound healing,[49] has strong adversary effects contributing to deep vein thrombosis,[50] cancer metastasis,[51] and COVID-19 pathology[52,53] makes targeting the molecular interactions leading to NET formation an important goal in biomedicine. One of the approaches to regulate or prevent NETosis would be to find a way of preventing PAD4-mediated chromatin unfolding by increasing free Mg^{2+} in neutrophils since a very small increase may efficiently preserve chromatin in the condensed state (Figure 2B). We expect that cryo-ET combined with nanoscale modeling should be an immense tool for detecting chromatin structural transitions underlying chromatin functions and a valuable resource for analysis of the convoluted chromatin path observed by EM or super-resolution microscopy *in situ*.

Limitations of the study

We note several limitations of the study resulting from the nature of cryo-ET imaging of isolated chromatin fragments embedded in vitrified ice. First, the thin ice layers, although essential for high-resolution cryo-ET, prevent analysis of larger nucleosome particles that are lost or damaged at the water/air interface. The nucleosome structures were visualized in the denoised images through the whole ice thickness, and the nucleosomes denatured by the water/air interface as well as fiduciary gold traces, and other impurities were excluded from structural analysis. Second, as in all studies of fragmented nucleosome arrays *in vitro*, the observed structures may be affected by a higher degree of structural freedom that destabilizes nucleosome folding *in vitro* and the absence of chromatin remodelers and other structural proteins that dynamically rearrange chromatin structure *in vivo*. We should note that previous studies of much longer condensed nucleosome arrays *in vitro* have resulted in regular 30 nm fibers that, in contrast to the multiplex folding observed here, clearly differ from the chromatin structures observed *in situ*, suggesting that a certain degree of structural freedom is needed to better recapitulate the multiplex organization of native chromatin. Third, the linkers (axes D) were not resolved for ~21% of all nucleosomes condensed by 0.75 mM Mg^{2+}, and corresponding angles α, β, and nucleosome interactions were excluded from the statistical analysis. Still, the internucleosomal distance N and angle *para* were recorded for all nucleosomes, and by comparing these variables between connected and unconnected nucleosomes (Figures S5P and S5Q), we found no evidence of nonrandom bias, suggesting that the missing densities were due to technical limitations of cryo-ET such as inherent noise and the missing wedge artifact. In the future, we plan to close this gap by optimizing data collection schemes, using advanced cryo-ET tomogram segmentation, denoising accounting for the missing wedge, and subtomogram averaging. Fourth, although we monitored the extent of histone citrullination, we have not determined the precise sites of histone citrullination and are aware that in native chromatin, various modifications can mutually interfere. In the future, we plan to use cryo-ET to address the folding of reconstituted chromatin containing predesigned and site-specific histone modifications.

STAR★METHODS

Detailed methods are provided in the online version of this paper and include the following:

- KEY RESOURCES TABLE
- RESOURCE AVAILABILITY
  - ○ Lead contact
  - ○ Materials availability
  - ○ Data and code availability
- EXPERIMENTAL MODEL AND STUDY PARTICIPANT DETAILS
- METHOD DETAILS
  - ○ Cells and tissue isolation
  - ○ Isolation of nuclei and native chromatin
  - ○ Reconstitution and biochemical analysis of the nucleosome arrays
  - ○ Mg^{2+}-dependent chromatin folding and self-association assays
  - ○ PAD4-treatment of chromatin samples
  - ○ Electrophoretic and Western blotting techniques
  - ○ Transmission Electron microscopy
  - ○ Cryo-Electron microscopy and tomographic reconstruction
  - ○ Regression tomogram denoising and 3D visualization
  - ○ Centroid/axis/plane (CAP) modeling of nucleosome chain folding
- QUANTIFICATION AND STATISTICAL ANALYSIS

SUPPLEMENTAL INFORMATION

Supplemental information can be found online at https://doi.org/10.1016/j.molcel.2023.08.017.

ACKNOWLEDGMENTS

We are thankful to J. Sloppy and H. Chen for technical assistance with electron microscopy at the Penn State Hershey Cryo-EM Facility (Facility SCR_021178) and TEM facility (RID: SCR_021200). We thank J. Buckwalter and L. Gautam (Penn State Hershey) for research assistance on earlier aspects of this project. Support for this work was provided to M.T.S. by NIH grant R01 NS126448-01A1 and S.A.G. by NSF grant 1911940 and by Pennsylvania Department of Health using Tobacco Settlement Funds grant 4100072562. The department specifically disclaims responsibility for any analyses, interpretations, or conclusions.

AUTHOR CONTRIBUTIONS

Conceptualization, S.A.G. and M.T.S.; methodology, M.T.S., S.A.G., and C.P.; investigation, N.J., B.K., and S.A.G.; formal analysis, N.J., B.K., and S.A.G.; writing – original draft, S.A.G.; writing – review & editing, N.J., C.P., B.K., and M.T.S.; funding acquisition, S.A.G.; resources, M.T.S. and S.A.G.; supervision, S.A.G. and M.T.S.

DECLARATION OF INTERESTS

The authors declare no competing interests.

INCLUSION AND DIVERSITY

We support inclusive, diverse, and equitable conduct of research.

Received: July 12, 2022
Revised: May 31, 2023
Accepted: August 16, 2023
Published: September 7, 2023

REFERENCES

1. Luger, K., Mäder, A.W., Richmond, R.K., Sargent, D.F., and Richmond, T.J. (1997). Crystal structure of the nucleosome core particle at 2.8 A resolution. Nature *389*, 251–260. https://doi.org/10.1038/38444.
2. Richmond, T.J., and Davey, C.A. (2003). The structure of DNA in the nucleosome core. Nature *423*, 145–150. https://doi.org/10.1038/nature01595.
3. Hu, Y., Kireev, I., Plutz, M., Ashourian, N., and Belmont, A.S. (2009). Large-scale chromatin structure of inducible genes: transcription on a condensed, linear template. J. Cell Biol. *185*, 87–100. https://doi.org/10.1083/jcb.200809196.
4. Alberts, B., Johnson, A., Lewis, J., Morgan, D., Raff, M., Roberts, K., and Walter, P. (2015). Molecular Biology of the Cell, Sixth Edition (Garland Science). https://doi.org/10.1201/9781315735368.
5. Poirier, M.G., Bussiek, M., Langowski, J., and Widom, J. (2008). Spontaneous access to DNA target sites in folded chromatin fibers. J. Mol. Biol. *379*, 772–786. https://doi.org/10.1016/j.jmb.2008.04.025.
6. Iwafuchi-Doi, M., and Zaret, K.S. (2014). Pioneer transcription factors in cell reprogramming. Genes Dev. *28*, 2679–2692. https://doi.org/10.1101/gad.253443.114.
7. Supek, F., and Lehner, B. (2015). Differential DNA mismatch repair underlies mutation rate variation across the human genome. Nature *521*, 81–84. https://doi.org/10.1038/nature14173.
8. Schneider, M.W.G., Gibson, B.A., Otsuka, S., Spicer, M.F.D., Petrovic, M., Blaukopf, C., Langer, C.C.H., Batty, P., Nagaraju, T., Doolittle, L.K., et al. (2022). A mitotic chromatin phase transition prevents perforation by microtubules. Nature *609*, 183–190. https://doi.org/10.1038/s41586-022-05027-y.
9. Woodcock, C.L., and Dimitrov, S. (2001). Higher order structure of chromatin and chromosomes. Curr. Opin. Genet. Dev. *11*, 130–135. https://doi.org/10.1016/s0959-437x(00)00169-6.
10. Scheffer, M.P., Eltsov, M., and Frangakis, A.S. (2011). Evidence for short-range helical order in the 30-nm chromatin fibers of erythrocyte nuclei. Proc. Natl. Acad. Sci. USA *108*, 16992–16997. https://doi.org/10.1073/pnas.1108268108.
11. Horowitz, R.A., Agard, D.A., Sedat, J.W., and Woodcock, C.L. (1994). The three-dimensional architecture of chromatin in situ: electron tomography reveals fibers composed of a continuously variable zig-zag nucleosomal ribbon. J. Cell Biol. *125*, 1–10. https://doi.org/10.1083/jcb.125.1.1.
12. Kizilyaprak, C., Spehner, D., Devys, D., and Schultz, P. (2010). In vivo chromatin organization of mouse rod photoreceptors correlates with histone modifications. PLoS One *5*, e11039. https://doi.org/10.1371/journal.pone.0011039.
13. Bednar, J., Horowitz, R.A., Grigoryev, S.A., Carruthers, L.M., Hansen, J.C., Koster, A.J., and Woodcock, C.L. (1998). Nucleosomes, linker DNA, and linker histone form a unique structural motif that directs the higher-order folding and compaction of chromatin. Proc. Natl. Acad. Sci. USA *95*, 14173–14178. https://doi.org/10.1073/pnas.95.24.14173.

14. Routh, A., Sandin, S., and Rhodes, D. (2008). Nucleosome repeat length and linker histone stoichiometry determine chromatin fiber structure. Proc. Natl. Acad. Sci. USA *105*, 8872–8877. https://doi.org/10.1073/pnas.0802336105.

15. Dorigo, B., Schalch, T., Kulangara, A., Duda, S., Schroeder, R.R., and Richmond, T.J. (2004). Nucleosome arrays reveal the two-start organization of the chromatin fiber. Science *306*, 1571–1573. https://doi.org/10.1126/science.1103124.

16. Schalch, T., Duda, S., Sargent, D.F., and Richmond, T.J. (2005). X-ray structure of a tetranucleosome and its implications for the chromatin fibre. Nature *436*, 138–141. https://doi.org/10.1038/nature03686.

17. Song, F., Chen, P., Sun, D., Wang, M., Dong, L., Liang, D., Xu, R.M., Zhu, P., and Li, G. (2014). Cryo-EM study of the chromatin fiber reveals a double helix twisted by tetranucleosomal units. Science *344*, 376–380. https://doi.org/10.1126/science.1251413.

18. Garcia-Saez, I., Menoni, H., Boopathi, R., Shukla, M.S., Soueidan, L., Noirclerc-Savoye, M., Le Roy, A., Skoufias, D.A., Bednar, J., Hamiche, A., et al. (2018). Structure of an H1-bound 6-nucleosome array reveals an untwisted two-start chromatin fiber conformation. Mol. Cell *72*, 902–915.e7. https://doi.org/10.1016/j.molcel.2018.09.027.

19. Soman, A., Wong, S.Y., Korolev, N., Surya, W., Lattmann, S., Vogirala, V.K., Chen, Q., Berezhnoy, N.V., van Noort, J., Rhodes, D., and Nordenskiold, L. (2022). Columnar structure of human telomeric chromatin. Nature *609*, 1048–1055. https://doi.org/10.1038/s41586-022-05236-5.

20. Joti, Y., Hikima, T., Nishino, Y., Kamada, F., Hihara, S., Takata, H., Ishikawa, T., and Maeshima, K. (2012). Chromosomes without a 30-nm chromatin fiber. Nucleus *3*, 404–410. https://doi.org/10.4161/nucl.21222.

21. Luger, K., Dechassa, M.L., and Tremethick, D.J. (2012). New insights into nucleosome and chromatin structure: an ordered state or a disordered affair? Nat. Rev. Mol. Cell Biol. *13*, 436–447. https://doi.org/10.1038/nrm3382.

22. Grigoryev, S.A. (2018). Chromatin higher-order folding: A perspective with linker DNA angles. Biophys. J. *114*, 2290–2297. https://doi.org/10.1016/j.bpj.2018.03.009.

23. Fussner, E., Ching, R.W., and Bazett-Jones, D.P. (2011). Living without 30nm chromatin fibers. Trends Biochem. Sci. *36*, 1–6. https://doi.org/10.1016/j.tibs.2010.09.002.

24. Eltsov, M., Maclellan, K.M., Maeshima, K., Frangakis, A.S., and Dubochet, J. (2008). Analysis of cryo-electron microscopy images does not support the existence of 30-nm chromatin fibers in mitotic chromosomes in situ. Proc. Natl. Acad. Sci. USA *105*, 19732–19737. https://doi.org/10.1073/pnas.0810057105.

25. Ou, H.D., Phan, S., Deerinck, T.J., Thor, A., Ellisman, M.H., and O'Shea, C.C. (2017). ChromEMT: visualizing 3D chromatin structure and compaction in interphase and mitotic cells. Science *357*, 370. https://doi.org/10.1126/science.aag0025.

26. Cai, S., Chen, C., Tan, Z.Y., Huang, Y., Shi, J., and Gan, L. (2018). Cryo-ET reveals the macromolecular reorganization of S. pombe mitotic chromosomes in vivo. Proc. Natl. Acad. Sci. USA *115*, 10977–10982. https://doi.org/10.1073/pnas.1720476115.

27. Ricci, M.A., Manzo, C., García-Parajo, M.F., Lakadamyali, M., and Cosma, M.P. (2015). Chromatin fibers are formed by heterogeneous groups of nucleosomes in vivo. Cell *160*, 1145–1158. https://doi.org/10.1016/j.cell.2015.01.054.

28. Nozaki, T., Imai, R., Tanbo, M., Nagashima, R., Tamura, S., Tani, T., Joti, Y., Tomita, M., Hibino, K., Kanemaki, M.T., et al. (2017). Dynamic organization of chromatin domains revealed by super-resolution live-cell imaging. Mol. Cell *67*, 282–293.e7. https://doi.org/10.1016/j.molcel.2017.06.018.

29. Maeshima, K., Rogge, R., Tamura, S., Joti, Y., Hikima, T., Szerlong, H., Krause, C., Herman, J., Seidel, E., DeLuca, J., et al. (2016). Nucleosomal arrays self-assemble into supramolecular globular structures lacking 30-nm fibers. EMBO J. *35*, 1115–1132. https://doi.org/10.15252/embj.201592660.

30. Gibson, B.A., Doolittle, L.K., Schneider, M.W.G., Jensen, L.E., Gamarra, N., Henry, L., Gerlich, D.W., Redding, S., and Rosen, M.K. (2019). Organization of chromatin by intrinsic and regulated phase separation. Cell *179*, 470–484.e21. https://doi.org/10.1016/j.cell.2019.08.037.

31. Strickfaden, H., Tolsma, T.O., Sharma, A., Underhill, D.A., Hansen, J.C., and Hendzel, M.J. (2020). Condensed chromatin behaves like a solid on the mesoscale in vitro and in living cells. Cell *183*, 1772–1784.e13. https://doi.org/10.1016/j.cell.2020.11.027.

32. Gibson, B.A., Blaukopf, C., Lou, T., Chen, L., Doolittle, L.K., Finkelstein, I., Narlikar, G.J., Gerlich, D.W., and Rosen, M.K. (2023). In diverse conditions, intrinsic chromatin condensates have liquid-like material properties. Proc. Natl. Acad. Sci. USA *120*, e2218085120. https://doi.org/10.1073/pnas.2218085120.

33. Grigoryev, S.A., Bascom, G., Buckwalter, J.M., Schubert, M.B., Woodcock, C.L., and Schlick, T. (2016). Hierarchical looping of zigzag nucleosome chains in metaphase chromosomes. Proc. Natl. Acad. Sci. USA *113*, 1238–1243. https://doi.org/10.1073/pnas.1518280113.

34. Risca, V.I., Denny, S.K., Straight, A.F., and Greenleaf, W.J. (2017). Variable chromatin structure revealed by in situ spatially correlated DNA cleavage mapping. Nature *541*, 237–241. https://doi.org/10.1038/nature20781.

35. Krietenstein, N., Abraham, S., Venev, S.V., Abdennur, N., Gibcus, J., Hsieh, T.S., Parsi, K.M., Yang, L., Maehr, R., Mirny, L.A., et al. (2020). Ultrastructural details of mammalian chromosome architecture. Mol. Cell *78*, 554–565.e7. https://doi.org/10.1016/j.molcel.2020.03.003.

36. Hsieh, T.S., Cattoglio, C., Slobodyanyuk, E., Hansen, A.S., Rando, O.J., Tjian, R., and Darzacq, X. (2020). Resolving the 3D landscape of transcription-linked mammalian chromatin folding. Mol. Cell *78*, 539–553.e8. https://doi.org/10.1016/j.molcel.2020.03.002.

37. Fang, K., Chen, X., Li, X., Shen, Y., Sun, J., Czajkowsky, D.M., and Shao, Z. (2018). Super-resolution imaging of individual human subchromosomal regions in situ reveals nanoscopic building blocks of higher-order structure. ACS Nano *12*, 4909–4918. https://doi.org/10.1021/acsnano.8b01963.

38. Kieffer-Kwon, K.R., Nimura, K., Rao, S.S.P., Xu, J., Jung, S., Pekowska, A., Dose, M., Stevens, E., Mathe, E., Dong, P., et al. (2017). Myc regulates chromatin decompaction and nuclear architecture during B cell activation. Mol. Cell *67*, 566–578.e10. https://doi.org/10.1016/j.molcel.2017.07.013.

39. Saibil, H.R. (2022). Cryo-EM in molecular and cellular biology. Mol. Cell *82*, 274–284. https://doi.org/10.1016/j.molcel.2021.12.016.

40. Hylton, R.K., and Swulius, M.T. (2021). Challenges and triumphs in cryo-electron tomography. iScience *24*, 102959. https://doi.org/10.1016/j.isci.2021.102959.

41. Mahamid, J., Pfeffer, S., Schaffer, M., Villa, E., Danev, R., Cuellar, L.K., Förster, F., Hyman, A.A., Plitzko, J.M., and Baumeister, W. (2016). Visualizing the molecular sociology at the HeLa cell nuclear periphery. Science *351*, 969–972. https://doi.org/10.1126/science.aad8857.

42. Cai, S., Böck, D., Pilhofer, M., and Gan, L. (2018). The in situ structures of mono-, di-, and tri-nucleosomes in human heterochromatin. Mol. Biol. Cell *29*, 2450–2457. https://doi.org/10.1091/mbc.E18-05-0331.

43. Eltsov, M., Grewe, D., Lemercier, N., Frangakis, A., Livolant, F., and Leforestier, A. (2018). Nucleosome conformational variability in solution and in interphase nuclei evidenced by cryo-electron microscopy of vitreous sections. Nucleic Acids Res. *46*, 9189–9200. https://doi.org/10.1093/nar/gky670.

44. Xu, P., Mahamid, J., Dombrowski, M., Baumeister, W., Olins, A.L., and Olins, D.E. (2021). Interphase epichromatin: last refuge for the 30-nm chromatin fiber? Chromosoma *130*, 91–102. https://doi.org/10.1007/s00412-021-00759-8.

45. Arimura, Y., Shih, R.M., Froom, R., and Funabiki, H. (2021). Structural features of nucleosomes in interphase and metaphase chromosomes. Mol. Cell *81*, 4377–4397.e12. https://doi.org/10.1016/j.molcel.2021.08.010.

46. Grigoryev, S.A., Bednar, J., and Woodcock, C.L. (1999). MENT, a heterochromatin protein that mediates higher order chromatin folding, is a new serpin family member. J. Biol. Chem. *274*, 5626–5636. https://doi.org/10.1074/jbc.274.9.5626.

47. Beel, A.J., Azubel, M., Matteï, P.J., and Kornberg, R.D. (2021). Structure of mitotic chromosomes. Mol. Cell *81*, 4369–4376.e3. https://doi.org/10.1016/j.molcel.2021.08.020.

48. Wang, Y., Li, M., Stadler, S., Correll, S., Li, P., Wang, D., Hayama, R., Leonelli, L., Han, H., Grigoryev, S.A., et al. (2009). Histone hypercitrullination mediates chromatin decondensation and neutrophil extracellular trap formation. J. Cell Biol. *184*, 205–213. https://doi.org/10.1083/jcb.200806072.

49. Brinkmann, V., and Zychlinsky, A. (2012). Neutrophil extracellular traps: is immunity the second function of chromatin? J. Cell Biol. *198*, 773–783. https://doi.org/10.1083/jcb.201203170.

50. Martinod, K., Demers, M., Fuchs, T.A., Wong, S.L., Brill, A., Gallant, M., Hu, J., Wang, Y., and Wagner, D.D. (2013). Neutrophil histone modification by peptidylarginine deiminase 4 is critical for deep vein thrombosis in mice. Proc. Natl. Acad. Sci. USA *110*, 8674–8679. https://doi.org/10.1073/pnas.1301059110.

51. Yang, L., Liu, Q., Zhang, X., Liu, X., Zhou, B., Chen, J., Huang, D., Li, J., Li, H., Chen, F., et al. (2020). DNA of neutrophil extracellular traps promotes cancer metastasis via CCDC25. Nature *583*, 133–138. https://doi.org/10.1038/s41586-020-2394-6.

52. Veras, F.P., Pontelli, M.C., Silva, C.M., Toller-Kawahisa, J.E., de Lima, M., Nascimento, D.C., Schneider, A.H., Caetité, D., Tavares, L.A., Paiva, I.M., et al. (2020). SARS-CoV-2-triggered neutrophil extracellular traps mediate COVID-19 pathology. J. Exp. Med. *217*, e20201129. https://doi.org/10.1084/jem.20201129.

53. Barnes, B.J., Adrover, J.M., Baxter-Stoltzfus, A., Borczuk, A., Cools-Lartigue, J., Crawford, J.M., Daßler-Plenker, J., Guerci, P., Huynh, C., Knight, J.S., et al. (2020). Targeting potential drivers of COVID-19: neutrophil extracellular traps. J. Exp. Med. *217*, e20200652. https://doi.org/10.1084/jem.20200652.

54. Maeshima, K., Matsuda, T., Shindo, Y., Imamura, H., Tamura, S., Imai, R., Kawakami, S., Nagashima, R., Soga, T., Noji, H., et al. (2018). A transient rise in free Mg(2+) ions released from ATP-Mg hydrolysis contributes to mitotic chromosome condensation. Curr. Biol. *28*, 444–451.e6. https://doi.org/10.1016/j.cub.2017.12.035.

55. Carruthers, L.M., Bednar, J., Woodcock, C.L., and Hansen, J.C. (1998). Linker histones stabilize the intrinsic salt-dependent folding of nucleosomal arrays: mechanistic ramifications for higher-order chromatin folding. Biochemistry *37*, 14776–14787. https://doi.org/10.1021/bi981684e.

56. Kremer, J.R., Mastronarde, D.N., and McIntosh, J.R. (1996). Computer visualization of three-dimensional image data using IMOD. J. Struct. Biol. *116*, 71–76. https://doi.org/10.1006/jsbi.1996.0013.

57. D'Imprima, E., Floris, D., Joppe, M., Sánchez, R., Grininger, M., and Kühlbrandt, W. (2019). Protein denaturation at the air-water interface and how to prevent it. eLife *8*, e42747. https://doi.org/10.7554/eLife.42747.

58. Correll, S.J., Schubert, M.H., and Grigoryev, S.A. (2012). Short nucleosome repeats impose rotational modulations on chromatin fibre folding. EMBO J. *31*, 2416–2426. https://doi.org/10.1038/emboj.2012.80.

59. Popova, E.Y., Grigoryev, S.A., Fan, Y., Skoultchi, A.I., Zhang, S.S., and Barnstable, C.J. (2013). Developmentally regulated linker histone H1c promotes heterochromatin condensation and mediates structural integrity of rod photoreceptors in mouse retina. J. Biol. Chem. *288*, 17895–17907. https://doi.org/10.1074/jbc.M113.452144.

60. Purnell, C., Heebner, J., Swulius, M.T., Hylton, R., Kabonick, S., Grillo, M., Grigoryev, S., Heberle, F., Waxham, M.N., and Swulius, M.T. (2023). Rapid synthesis of cryo-ET data for training deep learning models. https://doi.org/10.1101/2023.04.28.538636.

61. Pettersen, E.F., Goddard, T.D., Huang, C.C., Couch, G.S., Greenblatt, D.M., Meng, E.C., and Ferrin, T.E. (2004). UCSF Chimera–a visualization system for exploratory research and analysis. J. Comput. Chem. *25*, 1605–1612. https://doi.org/10.1002/jcc.20084.

62. Tsunaka, Y., Kajimura, N., Tate, S., and Morikawa, K. (2005). Alteration of the nucleosomal DNA path in the crystal structure of a human nucleosome core particle. Nucleic Acids Res. *33*, 3424–3434. https://doi.org/10.1093/nar/gki663.

63. Strauss, F., and Prunell, A. (1982). Nucleosome spacing in rat liver chromatin. A study with exonuclease III. Nucleic Acids Res. *10*, 2275–2293. https://doi.org/10.1093/nar/10.7.2275.

64. Widom, J. (1992). A relationship between the helical twist of DNA and the ordered positioning of nucleosomes in all eukaryotic cells. Proc. Natl. Acad. Sci. USA *89*, 1095–1099. https://doi.org/10.1073/pnas.89.3.1095.

65. Baldi, S., Krebs, S., Blum, H., and Becker, P.B. (2018). Genome-wide measurement of local nucleosome array regularity and spacing by nanopore sequencing. Nat. Struct. Mol. Biol. *25*, 894–901. https://doi.org/10.1038/s41594-018-0110-0.

66. Grigoryev, S.A., Arya, G., Correll, S., Woodcock, C.L., and Schlick, T. (2009). Evidence for heteromorphic chromatin fibers from analysis of nucleosome interactions. Proc. Natl. Acad. Sci. USA *106*, 13317–13322. https://doi.org/10.1073/pnas.0903280106.

67. Finch, J.T., and Klug, A. (1976). Solenoidal model for superstructure in chromatin. Proc. Natl. Acad. Sci. USA *73*, 1897–1901. https://doi.org/10.1073/pnas.73.6.1897.

68. Grigoryev, S.A. (2004). Keeping fingers crossed: heterochromatin spreading through interdigitation of nucleosome arrays. FEBS Lett. *564*, 4–8. https://doi.org/10.1016/S0014-5793(04)00258-3.

69. Chicano, A., Crosas, E., Otón, J., Melero, R., Engel, B.D., and Daban, J.R. (2019). Frozen-hydrated chromatin from metaphase chromosomes has an interdigitated multilayer structure. EMBO J. *38*, e99769. https://doi.org/10.15252/embj.201899769.

70. Pepenella, S., Murphy, K.J., and Hayes, J.J. (2014). Intra- and inter-nucleosome interactions of the core histone tail domains in higher-order chromatin structure. Chromosoma *123*, 3–13. https://doi.org/10.1007/s00412-013-0435-8.

71. Ghoneim, M., Fuchs, H.A., and Musselman, C.A. (2021). Histone tail conformations: A fuzzy affair with DNA. Trends Biochem. Sci. *46*, 564–578. https://doi.org/10.1016/j.tibs.2020.12.012.

72. Salzberg, A.C., Harris-Becker, A., Popova, E.Y., Keasey, N., Loughran, T.P., Claxton, D.F., and Grigoryev, S.A. (2017). Genome-wide mapping of histone H3K9me2 in acute myeloid leukemia reveals large chromosomal domains associated with massive gene silencing and sites of genome instability. PLoS One *12*, e0173723. https://doi.org/10.1371/journal.pone.0173723.

73. Wang, Y., Wysocka, J., Sayegh, J., Lee, Y.H., Perlin, J.R., Leonelli, L., Sonbuchner, L.S., McDonald, C.H., Cook, R.G., Dou, Y., et al. (2004). Human PAD4 regulates histone arginine methylation levels via demethylimination. Science *306*, 279–283. https://doi.org/10.1126/science.1101400.

74. Shechter, D., Dormann, H.L., Allis, C.D., and Hake, S.B. (2007). Extraction, purification and analysis of histones. Nat. Protoc. *2*, 1445–1457. https://doi.org/10.1038/nprot.2007.202.

75. Bass, M.V., Nikitina, T., Norouzi, D., Zhurkin, V.B., and Grigoryev, S.A. (2019). Nucleosome spacing periodically modulates nucleosome chain folding and DNA topology in circular nucleosome arrays. J. Biol. Chem. *294*, 4233–4246. https://doi.org/10.1074/jbc.RA118.006412.

76. Grigoryev, S.A. (2012). Nucleosome spacing and chromatin higher-order folding. Nucleus *3*, 493–499. https://doi.org/10.4161/nucl.22168.

77. Woodcock, C.L., Skoultchi, A.I., and Fan, Y. (2006). Role of linker histone in chromatin structure and function: H1 stoichiometry and nucleosome repeat length. Chromosome Res. *14*, 17–25. https://doi.org/10.1007/s10577-005-1024-3.

78. Thorn, G.J., Clarkson, C.T., Rademacher, A., Mamayusupova, H., Schotta, G., Rippe, K., and Teif, V.B. (2022). DNA sequence-dependent formation of heterochromatin nanodomains. Nat. Commun. *13*, 1861. https://doi.org/10.1038/s41467-022-29360-y.

79. Otterstrom, J., Castells-Garcia, A., Vicario, C., Gomez-Garcia, P.A., Cosma, M.P., and Lakadamyali, M. (2019). Super-resolution microscopy reveals how histone tail acetylation affects DNA compaction within nucleosomes in vivo. Nucleic Acids Res. *47*, 8470–8484. https://doi.org/10.1093/nar/gkz593.

80. Collepardo-Guevara, R., and Schlick, T. (2014). Chromatin fiber polymorphism triggered by variations of DNA linker lengths. Proc. Natl. Acad. Sci. USA *111*, 8061–8066. https://doi.org/10.1073/pnas.1315872111.

81. Skrajna, A., Goldfarb, D., Kedziora, K.M., Cousins, E.M., Grant, G.D., Spangler, C.J., Barbour, E.H., Yan, X., Hathaway, N.A., Brown, N.G., et al. (2020). Comprehensive nucleosome interactome screen establishes fundamental principles of nucleosome binding. Nucleic Acids Res. *48*, 9415–9432. https://doi.org/10.1093/nar/gkaa544.

82. Brouwer, T., Pham, C., Kaczmarczyk, A., de Voogd, W.J., Botto, M., Vizjak, P., Mueller-Planitz, F., and van Noort, J. (2021). A critical role for linker DNA in higher-order folding of chromatin fibers. Nucleic Acids Res. *49*, 2537–2551. https://doi.org/10.1093/nar/gkab058.

83. Dombrowski, M., Engeholm, M., Dienemann, C., Dodonova, S., and Cramer, P. (2022). Histone H1 binding to nucleosome arrays depends on linker DNA length and trajectory. Nat. Struct. Mol. Biol. *29*, 493–501. https://doi.org/10.1038/s41594-022-00768-w.

84. Narlikar, G.J., Sundaramoorthy, R., and Owen-Hughes, T. (2013). Mechanisms and functions of ATP-dependent chromatin-remodeling enzymes. Cell *154*, 490–503. https://doi.org/10.1016/j.cell.2013.07.011.

85. Dwiranti, A., Takata, H., and Fukui, K. (2019). Reversible changes of chromosome structure upon different concentrations of divalent cations. Microsc. Microanal. *25*, 817–821. https://doi.org/10.1017/S1431927619000266.

86. Nishikawa, J., and Ohyama, T. (2013). Selective association between nucleosomes with identical DNA sequences. Nucleic Acids Res. *41*, 1544–1554. https://doi.org/10.1093/nar/gks1269.

87. Ohyama, T. (2019). New aspects of magnesium function: A key regulator in nucleosome self-assembly, chromatin folding and phase separation. Int. J. Mol. Sci. *20*, 4232. https://doi.org/10.3390/ijms20174232.

88. Korolev, N., Lyubartsev, A.P., and Nordenskiöld, L. (2018). A systematic analysis of nucleosome core particle and nucleosome-nucleosome stacking structure. Sci. Rep. *8*, 1543. https://doi.org/10.1038/s41598-018-19875-0.

89. Kujirai, T., Horikoshi, N., Sato, K., Maehara, K., Machida, S., Osakabe, A., Kimura, H., Ohkawa, Y., and Kurumizaka, H. (2016). Structure and function of human histone H3.Y nucleosome. Nucleic Acids Res. *44*, 6127–6141. https://doi.org/10.1093/nar/gkw202.

90. Lukášová, E., Kořistek, Z., Klabusay, M., Ondřej, V., Grigoryev, S., Bačíková, A., Řezáčová, M., Falk, M., Vávrová, J., Kohútová, V., et al. (2013). Granulocyte maturation determines ability to release chromatin NETs and loss of DNA damage response; these properties are absent in immature AML granulocytes. Biochim. Biophys. Acta *1833*, 767–779. https://doi.org/10.1016/j.bbamcr.2012.12.012.

91. Gößwein, S., Lindemann, A., Mahajan, A., Maueröder, C., Martini, E., Patankar, J., Schett, G., Becker, C., Wirtz, S., Naumann-Bartsch, N., et al. (2019). Citrullination licenses calpain to decondense nuclei in neutrophil extracellular trap formation. Front. Immunol. *10*, 2481. https://doi.org/10.3389/fimmu.2019.02481.

92. Thiam, H.R., Wong, S.L., Qiu, R., Kittisopikul, M., Vahabikashi, A., Goldman, A.E., Goldman, R.D., Wagner, D.D., and Waterman, C.M. (2020). NETosis proceeds by cytoskeleton and endomembrane disassembly and PAD4-mediated chromatin decondensation and nuclear envelope rupture. Proc. Natl. Acad. Sci. USA *117*, 7326–7337. https://doi.org/10.1073/pnas.1909546117.

93. Schneider, C.A., Rasband, W.S., and Eliceiri, K.W. (2012). NIH Image to ImageJ: 25 years of image analysis. Nat. Methods *9*, 671–675. https://doi.org/10.1038/nmeth.2089.

94. Laemmli, U.K. (1970). Cleavage of structural proteins during the assembly of the head of bacteriophage T4. Nature *227*, 680–685. https://doi.org/10.1038/227680a0.

95. Popova, E.Y., Krauss, S.W., Short, S.A., Lee, G., Villalobos, J., Etzell, J., Koury, M.J., Ney, P.A., Chasis, J.A., and Grigoryev, S.A. (2009). Chromatin condensation in terminally differentiating mouse erythroblasts does not involve special architectural proteins but depends on histone deacetylation. Chromosome Res. *17*, 47–64. https://doi.org/10.1007/s10577-008-9005-y.

96. Sidoli, S., Bhanu, N.V., Karch, K.R., Wang, X., and Garcia, B.A. (2016). Complete workflow for analysis of histone post-translational modifications using bottom-up mass spectrometry: from histone extraction to data analysis. J. Vis. Exp.54112 https://doi.org/10.3791/54112.

97. Woodcock, C.L., and Horowitz, R.A. (1998). Electron microscopic imaging of chromatin with nucleosome resolution. Methods Cell Biol. *53*, 167–186. https://doi.org/10.1016/s0091-679x(08)60879-1.

STAR★METHODS

KEY RESOURCES TABLE

REAGENT or RESOURCE	SOURCE	IDENTIFIER
Antibodies		
H3 citrullinated at Arginine 2, 8, and 17	Abcam	Cat# ab5103; RRID: AB_304752
anti-rabbit HRP-conjugated	Abcam	Cat# ab205718; RRID:AB_2819160
Bacterial and virus strains		
E. coli DH5α	Invitrogen	Cat# 18265017
Biological samples		
Gallus gallus core histone octamers	Bass et al.[75] Isolated from chicken erythrocyte nuclei	N/A
Chemicals, peptides, and recombinant proteins		
RPMI 1640 medium +GlutaMAX™	Gibco	Cat# 61870-036
Fetal Bovine Serum	HyClone	Cat# SH30071
Penicillin/Streptomycin	Corning	Cat# 30-002-CI
NaCl	Sigma-Aldrich	Cat# S5150
$MgCl_2$	Sigma-Aldrich	Cat# M1028
HEPES	Avantor	Cat# 4018-04
Igepal CA-630 (Nonidet P-40)	Sigma-Aldrich	Cat# I3021
PMSF	Sigma-Aldrich	Cat# 78830
protease inhibitor cocktail	Sigma-Aldrich	Cat# P8849
phosphate buffered saline	Thermo Scientific	Cat# J62692
mimosine	Sigma Aldrich	Cat# M0253
hydroxyurea	Sigma Aldrich	Cat# H8627
micrococcal nuclease	Roche	Cat# 10107921001
$CaCl_2$	RICCA	Cat# R1760000
bovine serum albumin	New England Biolabs	Cat# B9001S
EDTA	Promega	Cat# 4231
Tris	VWR	Cat# 0497
Amicon ®Ultra-15 mL centrifugal filters	Millipore	Cat# UFC9050
Amicon ®Ultra-2 mL centrifugal filters	Millipore	Cat# UFC9024
Proteinase K	Thermo Scientific	Cat# EO0491
SDS	Bio-Rad	Cat# 161-0301
agarose	Lonza	Cat# 50000
Spectra/PorTM 1 RC Dialysis Membrane Tubing	SpectrumTM	Cat# 132650
linker histone variant $H1^0$	New England Biolabs	Cat# M2501S
$MgCl_2$	Sigma-Aldrich	Cat# M1028
glycerol	Fisher BioReagents	Cat# BP229-4
Ethidium Bromide	Bio Rad	Cat# 1610433
GelRed™	Biotium	Cat# 89139-138
human recombinant PAD4 enzyme	Sigma-Aldrich	Cat# SRP0329
human recombinant PAD4 enzyme	Cayman Chemical	Cat# 10500
DTT	Invitrogen	Cat# 15508-013
$NaHCO_3$	Fisher BioReagents	Cat# BP328
EGTA	RPI	Cat# E14100
acrylamide	Bio-Rad	Cat# 1610103
Bis-acrylamide	Fisher BioReagents	Cat# BP171
Brilliant blue R250	Fisher Biotech	Cat# BP101

(*Continued on next page*)

Continued

REAGENT or RESOURCE	SOURCE	IDENTIFIER
ECL prime Western detection kit	GE Healthcare	Cat# RPN2232
Triton X-100	MP	Cat# 194854
Acetic Acid	Fisher Scientific	Cat# A38-212
Urea	Merck	Cat# 108487
Trichloroacetic acid	Acros Organics	Cat# 42145
Methyl green	Sigma-Aldrich	Cat# M8884
Wizard SV Gel and PCR Clean-Up System	Promega	Cat# A9281
gel loading dye, no SDS	New England Biolabs	Cat# B7025S
1 kb DNA ladder	New England Biolabs	Cat# N3232
100 bp DNA ladders	New England Biolabs	Cat# N3231
agarose Type I-A, low EEO	Sigma-Aldrich	Cat# A0169
Tris/acetic acid/EDTA (TAE) buffer	Bio-Rad	Cat# 1610743
formaldehyde	Fisher Scientific	Cat# F79-500
agarose Type IV, special high EEO	Sigma-Aldrich	Cat# A3643
Glutaraldehyde 8%	Electron Microscopy Sciences	Cat# 16019
Deposited data		
Nucleosome core X-ray crystal structure	N/A	PDB: 2CV5
Raw tomogram tilt series (total: 64 *mrc files)	This paper; Dryad data depository https://datadryad.org	https://doi.org/10.5061/dryad.ttdz08m21
Chimera-based CAP models (total: 219 folders each containing one *.mrc file and one *.py file)	This paper; Dryad data depository https://datadryad.org	https://doi.org/10.5061/dryad.ttdz08m21
Original TEM, electrophoresis, and western blot images.	This paper; Mendeley Data https://data.mendeley.com	https://doi.org/10.17632/scnp36wvgr.1
Experimental models: Cell lines		
Human HeLa S3 cell line	ATCC	Cat# CCL-2.2
Human K562 cell line	ATCC	Cat# CCCL-243
Experimental models: Organisms/strains		
C57BL/6J mice	Jackson Laboratory	strain no. 000664
Recombinant DNA		
12x183 clone-601 DNA repeats in pUC19 vector	Bass et al.[75]	p-183X12
Software and algorithms		
Image J	Schneider et al.[93]	https://imagej.nih.gov/ij/
Prism 9	GraphPad	https://www.graphpad.com/updates/prism-931-release-notes
Tomography-5.7.1.	ThermoFisher	https://assets.thermofisher.com/TFS-Assets/MSD/Product-Updates/tomography-release-notes-307499.pdf
IMOD	Kremer et al.[56]	https://bio3d.colorado.edu/imod
UCSF CHIMERA	Pettersen et al.[61]	https://www.cgl.ucsf.edu/chimera/
cryo-TomoSim	Purnell et al.[60]	https://doi.org/10.5281/zenodo.8234233
Dragonfly	Object Research Systems	https://www.theobjects.com/dragonfly/index.html
Other		
carbon-coated EM grids	Electron Microscopy Sciences	Cat# CF400C-Cu
Quantifoil R2/2 200 mesh copper grids	Electron Microscopy Sciences	Cat# Q250-CR2
10 nm fiduciary gold particles	Sigma-Aldrich	Cat# 741957

RESOURCE AVAILABILITY

Lead contact

Further information and requests for resources and reagents should be directed to the lead contact, Sergei Grigoryev (sag17@psu.edu).

Materials availability

Materials are available from the lead contact upon request.

Data and code availability

- The cryo-EM image files (*.mrc) containing unprocessed cryo-EM tilt series listed in the Table S1 and the data folders containing Chimera model files (**.py) paired with cropped subtomogram files (**.mrc) listed in the Table S2 have been deposited on the Dryad data depository and are publicly available as of the date of publication. DOI is listed in the key resources table. Original electrophoretic and western blot images have been deposited at Mendeley and are publicly available as of the date of publication. DOI is listed in the key resources table. Microscopy data and processed tomograms reported in this paper will be shared by the lead contact upon request.
- All original code has been deposited at Zenodo and is publicly available as of the date of publication. DOI is listed in the key resources table.
- Any additional information required to reanalyze the data reported in this paper is available from the lead contact upon request.

EXPERIMENTAL MODEL AND STUDY PARTICIPANT DETAILS

Wild-type C57BL/6J mice were purchased from The Jackson Laboratory (strain no. 000664). This study was conducted with both male and female mice aged to post-natal day 21. All breeding and experimental procedures were carried out in accordance with the guidelines set by the National Institutes of Health's Office of Laboratory Animal Welfare and the National Science Foundation. All experiments were approved by the Penn State University College of Medicine (protocol no. 00929).

METHOD DETAILS

Cells and tissue isolation

Human K562 cells (ATCC CCCL-243) were grown at 37°C and 5% CO_2 in RPMI 1640 medium +GlutaMAX™ (Gibco 61870-036) supplemented with 10% FBS (HyClone SH30071) and Penicillin/Streptomycin (Corning cat.# 30-002-CI) in 600 mL (150 cm^2) tissue culture flasks with passing by dilution into new media every 72 hours. For preparative chromatin isolation, cells were grown in suspension until reaching density of 0.8-1.2 x 10^6 cells/mL to a final volume of 400 mL. The detached K562 cells were collected and twice washed by spinning down and resuspending in Phosphate Buffered Saline (PBS). To block the cell cycle in the G1 and S-phases, K562 cells were treated with 0.5 mM mimosine or 0.5 mM hydroxyurea for 24 hr. prior to nuclei isolation. For *in situ* chromatin crosslinking, K562 cells resuspended in PBS were treated by adding 0.3% formaldehyde for 10 min at room temperature and then twice washed by spinning down and resuspending in PBS. All subsequent procedures using the intact, cell-cycle blocked, and formaldehyde-crosslinked K562 cells were conducted under similar conditions.

Human HeLa S3 Cells (ATCC # CCL-2.2) were grown at +37°C and 5% CO_2 in RPMI 1640 medium +GlutaMAX™ (Gibco 61870-036) and 10% FBS (HyClone SH30071.03) in 10 cm^2 tissue culture plates with 10 mL of medium and passing by trypsinization and dilution into new media every 3-4 days. For preparative chromatin isolation, cells were grown to ca. 90% confluence in a final volume of 100 mL (10 plates), gently washed by pipetting with PBS, and detached by cell scraping in RSB buffer (10 mM NaCl, 3 mM $MgCl_2$, 10 mM HEPES, pH=7.5) containing 0.5% Nonidet P-40 (Igepal CA-630, Sigma I3021) in RSB, 1 mM PMSF, and protease inhibitor cocktail (Sigma P8849).

Mouse retina was collected for postnatal day 21 mice as previously described.[59] In particular, eyeballs were collected on ice and dissected to isolate retinas. 10–20 retinas were collected in 1 ml of cold PBS and triturated by pipetting up and down with a pipetman with a 1-ml tip. The suspension of cells was briefly spun down at 500 g for 3 min. For nuclei isolation cells were resuspended in 0.5% Igepal CA-630 in RSB plus 1 mM PMSF and protease inhibitor cocktail as above.

Isolation of nuclei and native chromatin

K562 and HeLa cell nuclei were isolated by resuspending the cells in 30 mL RSB buffer containing 0.5% Nonidet P-40, 1 mM PMSF, and protease inhibitor cocktail (Sigma P8849) at 4°C as described.[33] The cell suspensions were homogenized by 30 strokes of pestle B in a Dounce homogenizer over 30 min on ice. Nuclei were centrifuged for 5 min at 4,000 rpm and 4°C in an Eppendorf 5810 R centrifuge with an Eppendorf A-4-62 swinging bucket rotor, and the nuclear pellets were resuspended in 10 mL RSB plus 0.5 mM PMSF. Average yield for K562 and HeLa nuclei ~1 mg/mL and ~0.5-0.7 mg/mL of DNA, respectively, determined spectrophotometrically. The isolated nuclei were warmed at 37°C for 5 min and treated with micrococcal nuclease (MNase) (Roche 10107921001) and 2 mM

$CaCl_2$ (RICCA R1760000). MNase dilutions were prepared fresh before each digestion at 25 μg/mL in 1X bovine serum albumin (BSA) (New England Biolabs B9001S). Prepared MNase/BSA solution was then added to nuclei suspension at a dilution of 1:1000 and incubated for 60 minutes at 37°C in a Belly Dancer Orbital Shaker (IBI BDRAA115S) at 40-45 rpm to prepare chromatin fragments with a maximal median DNA size of ~2400 bp corresponding to 12 nucleosomes. The size of the nuclease fragments was determined by agarose DNA electrophoresis after DNA deproteinization by 1% SDS and 0.5 mg/ml proteinase K. The MNase digestion was stopped by adding 5 mM EDTA, rapidly cooling on ice, and spinning down for 5 min. at 10,000 rpm and 4°C in an Eppendorf 5810 R centrifuge with F-34-6-38 rotor. The nuclear pellet was resuspended in TE buffer (10 mM Tris, 1 mM EDTA, pH=8.0) and incubated at 4°C for 24-48 hr. with mild shaking at the start and end of incubation. The nuclear material was then centrifuged for 5 min. in the same manner at 10,000 rpm and 4°C. The supernatant (S2) containing soluble native chromatin was collected and the concentration of soluble DNA was monitored spectrophotometrically.

The released soluble chromatin S2 was concentrated on Amicon ®Ultra-15 mL centrifugal filters (Millipore UFC9050) to 0.35-0.5 mL with the final concentration ranging from 4.0-8.0 mg/mL. Concentrated chromatin samples were loaded on 11 mL gradients of 5-25% sucrose in TE buffer and centrifuged in a preparative ultracentrifuge with a SW41 Ti rotor (Beckman) for 11 hrs. at 35,000 rpm and 4°C. Aliquots of the sucrose gradient fractions were treated with 0.5 mg/mL Proteinase K in 1% SDS for 2 hr. at 55°C, and DNA analyzed by electrophoresis in 1% agarose (Lonza cat. # 50000) in TAE buffer as before.[33] Fractions enriched in particles with DNA sizes corresponding to 8–16 nucleosomes were collected, dialyzed for 48 hr. in a 1:250 ratio against HNE buffer (5 mM NaCl, 0.1 mM EDTA, 10 mM HEPES-NaOH, pH=7.5) in Spectra/PorTM 1 RC Dialysis Membrane Tubing (SpectrumTM 132650) and concentrated in Amicon ®Ultra-2 mL centrifugal filters (Millipore UFC205024).

Isolation of nuclei and native soluble chromatin from mouse retina tissue was carried out as previously described.[59] Specifically, retina cells were vortexed several times during a 20-min incubation on ice and then centrifuged 7 min at 3,500 g and 4°C in an Eppendorf 5810 R centrifuge with F-34-6-38 rotor. Nuclei were resuspended in RSB plus 1 mM PMSF and a protease inhibitor mixture (Sigma). Isolation of soluble chromatin (S2) was conducted as described above for K562 cells.

Reconstitution and biochemical analysis of the nucleosome arrays

Procedures for construction of DNA templates (183x12) for multimeric oligonucleosome arrays, their reconstitution with core histone octamers by salt dialysis, agarose gel electrophoresis, restriction enzyme protection, analytical ultracentrifugation, and electron microscopy to verify the correct number and positioning of the nucleosome cores are as described in.[75] Additional reconstitutions with linker histone were performed by mixing reconstituted 183x12 core arrays with 1 mg/ml recombinant linker histone variant $H1^0$ (New England Biolabs, cat.# M2501S) at a molar ratio of 0.7 molecule histone H1 per nucleosome in solution containing 500 mM NaCl, 10 mM HEPES, 0.1 mM EDTA and dialyzing against HNE buffer as described.[33]

Mg^{2+}-dependent chromatin folding and self-association assays

Native and reconstituted nucleosome arrays were dissolved in HNE buffer at final concentrations of 100 and 200 μg/mL for chromatin self-association assays and imaging analyses, respectively, and mixed with increasing concentrations of $MgCl_2$ (Sigma Aldrich, cat. # M1028-1mL) and incubated for 20 minutes on ice. For some experiments, samples were incubated for up to 48 hrs. and used for further imaging or electrophoretic experiments.

The extent of chromatin self-association was analyzed using selective precipitation in magnesium as described.[75] The chromatin samples were incubated for 20 min. at different concentrations of $MgCl_2$, and centrifuged at 12,000 rpm, 4°C, for 10 min in an Eppendorf 5810 R centrifuge with an F-34-6-38 rotor. Supernatants were collected and mixed with and equal volume of 12% glycerol, 40 mM EDTA, 2% SDS; the pellets were resuspended in 8% glycerol, 10 mM EDTA, 1% SDS. DNA from supernatants and pellets were analyzed on 1% agarose (Lonza cat. # 50000) gels in TAE buffer at 3 V/cm for 40 min. and stained with Ethidium Bromide (Fisher BioReagents FL-07-0702) or GelRedTM (VWR 89139-138). The percentage of DNA in the supernatant and pellet was determined by DNA band quantification using Image J software.[93] The percentages of DNA at increasing $MgCl_2$ concentration were input into Prism 9 for MacOS in order to interpolate a standard curve (Sigmoidal, 4PL, X is concentration) for both supernatant and pellet fractions. The IC50 values were used to determine the average concentration of $MgCl_2$ at which 50% of the native or reconstituted chromatin was precipitated.

PAD4-treatment of chromatin samples

To induce histone citrullination, the native or reconstituted chromatin samples (140 μg DNA/ml) in HNE were treated with 25 μg/ml human recombinant PAD4 enzyme (Sigma Aldrich cat # SRP0329 or Cayman Chemical cat. # 10500), 2.3 mM DTT, 1.9 mM $CaCl_2$, 0.5 mM PMSF, and 25 mM $NaHCO_3$. Control samples received the same treatment minus PAD4 or $CaCl_2$. The PAD4-treated and control samples were incubated at 37°C for 1-2 hr. followed by 2 mM EGTA and placed on ice to stop the reaction. Histone citrullination was monitored by SDS-PAGE electrophoresis showing the downward mobility shifts of histone H3 and H4 and H1 due to its citrullination[73] and by Western blotting with antibodies against citrullinated histone H3 (Abcam ab5103).

Electrophoretic and Western blotting techniques

For SDS-PAGE electrophoresis of control and PAD4 treated histones and band-shift analysis of citrullinated histones chromatin samples were dissolved in SDS-containing loading buffer and the electrophoresis was carried out in 18% acrylamide gels as described.[94] The gels were stained with Brilliant blue R250 (FisherBiotech FL-04-0598).

For SDS-PAGE electrophoresis followed by Western blotting, chromatin samples were dissolved in SDS-containing loading buffer and the electrophoresis was carried out in 8-16% mini-protean TGX Bio-Rad gels (Cat. # 4561105, Bio-Rad, Hercules, CA) gradient acrylamide gels as described.[94] Proteins were transferred to Immobilon-P PVDF membrane (Cat. #PVH00010 Millipore, Bedford, MA) as described[95] and detected with primary antibodies against H3 citrullinated at Arginine 2, 8, and 17 (dil. 1:5.000, cat.# ab5103, Abcam, UK), secondary goat anti-rabbit HRP-conjugated antibodies (dil. 1:40.000, cat.# ab205718; Abcam, UK) and ECL prime Western detection kit (cat. # RPN2232 GE Healthcare, UK)

For Triton-Acetic acid-Urea (TAU) electrophoresis[74] histones were acid-extracted from chromatin samples followed by precipitation with Trichloroacetic acid (TCA) as described.[96] Extracted histones were resuspended in ddH_2O and stored at -20°C until use. Concentration of extracted histones was approximated by serial dilution and SDS-PAGE electrophoresis in 18% acrylamide as before and compared relative to a protein control. TAU sample buffer (0.9 M acetic acid, 16% glycerol, 5 mM DTT, 5.8 M urea, methyl green) was prepared fresh prior to TAU gel electrophoresis. Aliquots of stored histones were prepared at 6-10 μg/sample and dried by speed vacuum and resuspended in 10 μL of TAU sample buffer. Short TAU separating gel was prepared as described[74] and placed in gel chamber with TAU running buffer (0.9 M acetic acid). Sample wells were flushed with running buffer using a syringe prior to loading samples. 10 μL of histones resuspended in sample buffer were loaded evenly into all lanes and run at 200 V constant for 2 hr. with the electrodes reversed. Lanes without sample received 10 μL of sample buffer. The gels were stained with Brilliant blue R250.

For high-resolution DNA electrophoresis resolving the nucleosome repeats genomic DNA was purified from chromatin samples using the Wizard SV Gel and PCR Clean-Up System (Promega, cat.# A9281) according to the manufacturer’s instructions. Samples were adjusted to a final concentration of 0.054 μg/μl with H_2O and one-sixth the final volume of gel loading dye, no SDS (New England Biolabs, cat.#. B7025S). For size reference 1 kb and 100 bp DNA ladders (New England Biolabs, cat.# N3232 and N3231) were combined and loaded onto the gel. The DNA samples were loaded to 0.49 ug and run on a 1.1% agarose gel (Sigma-Aldrich Type I-A, low EEO cat.# A0169) in 1x Tris/acetic acid/EDTA (TAE) buffer (Bio-Rad, cat.# 1610743) at 2.8 V/cm for 6 h 45 min with constant buffer recirculation. Gels were post-stained in GelRed and digitally imaged. Gel analysis was performed using Image J software[93] (National Institutes of Health) by measuring the relative migration distance (Rf) of the DNA standards and sample DNA bands. Rf values of the DNA standards were used to generate a standard curve of Rf against the log(Molecular weight) of the standards using Excel (Microsoft Excel for Office 365). The resulting linear equation was then used to determine the DNA length (bp) of each sample band. After determination of DNA length, the nucleosome repeat length was calculated as DNA length (bp) divided by the number of nucleosomes represented in each band. For DNP electrophoresis resolving the band shifts resulting from chromatin folding and self-association, we fixed the nucleosome arrays at 100–200 μg/mL with 0.4% formaldehyde for 10 min. on ice following 20 min incubation in HNE buffer containing various concentrations of $MgCl_2$. The fixed arrays were then mixed with 1/5 total volume of 50% glycerol/HE (20 mM HEPES, 0.1 mM EDTA), 12 mM EDTA, and subjected to deoxynucleoprotein (DNP) electrophoresis in 1.0% Type IV agarose (Sigma-Aldrich Type IV, special high EEO cat.# A3643) gel and run at 3 V/cm in HE buffer for 110 min. The agarose gels were stained by GelRed or ethidium bromide. Mendeley Data: https://data.mendeley.com/datasets/scnp36wvgr/1

Transmission Electron microscopy

For transmission electron microscopy, the samples resuspended in HNE containing appropriate concentrations of $MgCl_2$, were fixed with 0.1 % glutaraldehyde for 16 hr. and then dialyzed against HNE buffer. The dialyzed fixed samples were diluted to 1 μg/ml final concentration with 50mM NaCl, attached to carbon-coated and glow-discharged EM grids (EMS CF400C-Cu, Electron Microscopy Sciences), and stained with 2.0% uranyl acetate for negative staining.[97] Bright-field EM imaging was conducted at 200 kV using JEM-2100 electron microscope (JEOL USA, Peabody, MA) equipped with 4k x 4k Ultrascan CCD camera (Gatan Inc. Warrendale, PA). EM images were collected at 60 - 80K nominal magnification. Mendeley Data: https://data.mendeley.com/datasets/scnp36wvgr/1

Cryo-Electron microscopy and tomographic reconstruction

Chromatin samples incubated for 20 min. without or with appropriate concentrations of $MgCl_2$ were mixed with a suspension of 10 nm fiduciary gold particles (Sigma Aldrich cat.# 741957), which were coated in bovine serum albumin to prevent clustering. 3 μl chromatin samples with a concentration of about 0.2 mg/ml DNA were applied to Quantifoil R2/2 200 mesh copper grids (EMS Q250-CR2). Vitrification was conducted by plunging into liquid ethane using our FEI Vitrobot Mk IV Grid Plunging System at 100% humidity, 4°C, and setting the blotting strength at 5, and blotting time at 3.5 sec.

Imaging of the vitrified samples was conducted on Titan Krios G3i 300 kV electron microscope, equipped with a K3 direct electron detector (Gatan, CA) at the Penn State Hershey cryo-EM core. We used Tomography-5.7.1. software (Thermo Fisher) for controlling data acquisition and collecting tilt-series. Cryo-EM tilt series (± 60°) were collected at 5° intervals in dose symmetric mode, at either 2.2 angstroms/pixel (defocus -6 um) or 1.7 angstroms/pixel (defocus -5 um), with zero-loss peak energy filtration through a 20-eV slit. Images were collected in 1x counting mode. Each tilt series had a cumulative dose of 120 electrons/$Å^2$. Tilt series were aligned using fiducials in the IMOD[56] software suite (https://bio3d.colorado.edu/imod/), and reconstructed by Simultaneous Iterative Reconstruction Technique (SIRT) with contrast transfer function (CTF) correction. The chromatin samples, vitrification conditions, raw tilt series, and resulting cryotomograms are listed in the Table S1. The raw tilt series are available from Dryad data depository: https://datadryad.org; https://doi.org/10.5061/dryad.ttdz08m21.

Regression tomogram denoising and 3D visualization

Regression denoising was accomplished in Dragonfly (ORS) using data synthesized by cryo-TomoSim (CTS).[60] Zenodo repository: https://doi.org/10.5281/zenodo.8234233. To do this, CTS was given a broad set of atomic models (PDB: 1zbb, 5f99, 5oxv, 50y7, 6hkt, 6l4a, 6l49, 6la8, 6m3v, 7pet, 7peu, 7pev, 7pew, 7pex, 7pey, 7pf0, 7pfa, 7pft, 7v9k, 7va4) and was used to generate three 400x400x60 voxel models at each of the pixel sizes used to collect real data (8.4, 6.6, and 5.4 Angstroms/pixel for magnifications 42 kx, 53 kx, and 64 kx respectively). Particles were randomly chosen from the pool of structures and placed randomly within the volume so that no particles were overlapping. Each model was then used to simulate a pair of tomograms consisting of a noisy, CTF-corrupted instance as well as an ideal ''prior'' with no noise, missing wedge, or CTF corruption. Noise/Prior pairs were then provided as input and output, respectively, within Dragonfly to train regressive networks for denoising real tomograms at each of pixel sizes listed above. Networks were trained as 5-slice networks with a 64 pixel patch size or as full 3D networks with a patch size of 32 voxels cubed, a stride ratio of 1, batch size of 32 (or less), and the ''ORSMixedGradientLoss'' function. Training was run for 100 epochs or until there was no improvement in the loss function for 15 epochs. Real and simulated tomograms were then calibrated in Dragonfly so that the left tail of the histogram (dark pixels) was set to zero and the peak was set to 1000. Regression denoising was then accomplished in Dragonfly and then exported out as Tiff and converted to MRC using the *mrc2tif* program within IMOD. Data was visualized either with IMOD or Chimera.

Centroid/axis/plane (CAP) modeling of nucleosome chain folding

The reconstructed un-binned tomograms were visualized and segmented into smaller subtomograms by IMOD/3dmod. Each volume was inverted using ''newstack'' to generate subtomograms with positive intensity corresponding to high density and filtered using IMOD command: ''nad_eed_3d -n 30 -f -k 50'' to reduce noise and enhance chromatin edges. The filtered subtomograms were exported into UCSF Chimera[61] (RBVI, Univ. San Francisco, CA; https://www.cgl.ucsf.edu/chimera/) for interactive visualization and analysis of nucleosome structures. The air/water interface was examined in the denoised images so that any particles damaged at the air/water interface (yellow arrows on Figure S1) were excluded from the subsequent analysis. Since particles were often self-associated especially in crowded tomogram areas, for analysis of individual nucleosome arrays vitrified at 0 mM and at 0.75 mM Mg^2+we selected only free arrays or those that had no more than a single nucleosome contact to other particles and contained between 6 and 18 nucleosomes (see Table S2).

In Chimera, the filtered volumes were fitted with nucleosome core X-ray crystal structure (PDB: 2CV5[62]) semi-automatically to correspondent electron densities in the volume using the 'fitmap' command. The fitting of each nucleosome followed the local maximal electron density and thus was independent from the observer's bias. After fitting, the nucleosomes were overlaid with centroids selecting the centers of masses, center-to-center axes, and nucleosome planes crossing the nucleosome at the dyad axis using the structure analysis 'Axels/Planes/Centroids' tool. For stereological analysis, each nucleosome in an array was numbered, if possible, starting from one end of the array and numbering consecutive nucleosomes to the other end of the array. Where linkers were not visible (such as in the tertiary chromatin structures), the nucleosomes were labeled based on their spatial proximity. The following measurements were recorded from such Centroid-Axial-Plane (CAP) models for each nucleosome (n) in an array: a) center-to-center distance D to the next nucleosome (n+1) in the array, b) center-to-center distance N to the nearest nucleosome (n_x) in the 3D space, angle α between the two axes connecting each nucleosome with the previous one (n-1) and the next one (n+1) in a chain, angle β between the planes of consecutive nucleosomes n and n+1, and an angle *para* between the plane of each nucleosome (n) and the plane of the nearest nucleosome (n_x) in the 3D space (see Figure 3C). All distance and angle measurements for individual nucleosome arrays are included in the Table S2.

The absolute nucleosome pairwise proximity values were obtained by subtracting the number of each nucleosome (n) from the number of its nearest nucleosome (n_x) in the 3D space and calculating the absolute difference [n_x - n], see Table S2. Nucleosomes involved in interactions in ''trans'' were recorded when two nucleosomes from particles X and Y are in proximity and either the nucleosome in particle X is connected by two visible DNA linkers to other nucleosomes within the same particle or, when linker connections are missing, the unconnected nucleosomes in particles X and Y are at a distance of more than 30 nm (probability of physical connectivity at such distance is less than 1% from the analysis. The measured angle and plane values were analyzed statistically to determine the distribution profiles and average values that discriminate between the condensed and open nucleosomes arrays. Distance N and angle *para* were recorded for all nucleosomes. For some nucleosomes condensed by 0.75 mM Mg^{2+} (~21% of all nucleosomes) and for all nucleosomes condensed at > 1 mM Mg^{2+}, the linkers were not resolved and corresponding distances D and angles α and β were excluded from the statistical analysis.

QUANTIFICATION AND STATISTICAL ANALYSIS

Violin plots were generated using Prism vs. 9.5.1 (Graph Pad). All other plots were generated in Excel (Microsoft). Average and standard deviation values were obtained from at least three tomograms and at least two independent biological samples. *p*-values representing probability associated with a Student's two-sample unequal variance t-test with a two-tailed distribution are shown on the graphs; these values were calculated using Excel (Microsoft). Nonsignificant difference (ns) is shown for $p > 0.05$. Datasets with nonsignificant difference were additionally examined by nonparametric Kolmogorov-Smirnov test using Prism. In cases where the values are significant by Kolmogorov-Smirnov test but not by standard t-test (due to non-Gaussian distribution), the p-values resulting from the latter test are indicated by asterisks and are given in the corresponding figure legends. The numbers of nucleosomes (n) or nucleosome arrays (n') accounted for in each test are given in the corresponding figure legends.